LRP 374/89 February 1989

THE USE OF ALFVEN WAVES IN NET

G.G. Borg, K. Appert, A.J. Knight, J.B. Lister,
J. Vaclavik

Work done under **Contract No 251/86-10/FUCH/NET**

THE USE OF ALFVEN WAVES IN NET

G.G. BORG, K. APPERT, A.J. KNIGHT, J.B. LISTER and J. VACLAVIK
Centre de Recherches en Physique des Plasmas
Association EURATOM - Confédération Suisse
Ecole Polytechnique Fédérale de Lausanne
21, Av. des Bains, CH-1007 Lausanne, Switzerland

ABSTRACT

A number of features of Alfvén Wave Heating make it potentially attractive for use in large Tokamak reactors. Among them are the availability and relatively low cost of the power supplies, the potential ability to act selectively on the current profile, and the probable absence of operational limits in size, fields or density. The physics steps necessary to extrapolate our understanding of Alfvén Wave Heating to a large tokamak are assessed in this report.

Contract: No 251/86-10/FUCH/NET

CONTENTS

1. INTRODUCTION

Our understanding of Alfvén Wave Heating (AWH) has been gained from general theoretical studies, while experiments have been carried out in small devices, of which the largest is the TCA tokamak. The good qualitative agreement between AWH theory and experiment makes the possible application of AWH to a large device promising. However, we must be careful to identify any of the physics issues which are expected to be very different from those explored on TCA.

In this report we discuss areas of present knowledge, and then proceed to justify the extrapolation of the existing models to a large tokamak, taking the specific case of the NET design.

This report is arranged as follows. In Chapter 2 a brief outline of the existing theory of Alfvén Wave Heating is given, including a discussion of ideal and cold plasma MHD theory in 1- and 2-D, and of warm plasma theory in 1-D. The limitations of these theories are discussed, together with an assessment of their importance. The status of current theoretical research is described.

Experimental results on AWH are presented in Chapter 3. The main experimental results, chiefly from TCA but also from TORTUS, PRETEXT and R-O, will be briefly described and a bibliography will be given. The major outstanding questions concerning these results are addressed.

In Chapter 4 the properties of AWH which would be of benefit to NET are discussed, specifically the usefulness of AWH in the operational range of NET. The open questions are also specified.

In Chapter 5 we assess the physics of AWH in a large tokamak. Since the experimental results confirm only the behaviour of a small minor radius tokamak, this question is addressed in detail. Considerable attention is given to the scaling of the antenna loading, as it has been considered that one possible drawback of AWH is an unacceptably low plasma loading compared with residual losses. We show that this is not the case. Another difference in a large tokamak is the reduced antenna-wall and antenna-plasma spacing compared to the plasma minor radius. We find that

a large minor radius can enhance the antenna loading.

In Chapter 6 we show how the study presented in Chapter 5, together with the requirements of NET, lead naturally to a choice of optimal mode numbers and operating frequencies. Values of the antenna loading are estimated for a typical operational regime.

Having established the physics of an AWH system and nominal operating conditions, we address some practical issues in Chapter 7. The design of an antenna inside the torus is discussed, with the antenna recessed into the torus wall. This leads to a compromise between efficiency and protection of the recessed antenna. A typical circuit efficiency is estimated, with corresponding circulating currents for given delivered powers. Questions regarding tuning, feeds and power supplies are briefly considered.

Since NET requires additional heating/current-drive to operate over a wide range, we discuss in Chapter 8 the requirements of mode switching or re-tuning for optimisation.

Finally, a summary is presented in Chapter 9, drawing attention to outstanding issues which would require further study.

2. THEORY OF AWH

2.1 Outline of AWH and Bibliography

The principles of Alfvén Wave Heating (AWH) at frequencies below the ion cyclotron frequency, ω_{ci}, can be summarized as follows:

a) The Alfvén resonance layer (ARL) is defined, in cylindrical geometry, by the relation

$$\omega^2 = C_A^2(r_o)k_{||}^2(r_o)(1-\omega^2/\omega_{ci}^2) \qquad (2.1)$$

where $C_A(r)$ is the local Alfvén speed and $k_{||}(r)$ is the wavenumber parallel to the ambient magnetic field. The quantity $C_A(r)$ is given by $C_A(r) = B(r)/(m_o m_p <A> n_e(r))^{1/2}$, where B(r) is the local total steady magnetic field, $n_e(r)$ is the local plasma electron density, <A> is the plasma effective mass and m_p is the proton mass. From (2.1) it may be seen that the ARL exists in the plasma for a continuous range of frequencies or wavenumbers. This range is referred to as the Alfvén continuum. The minimum frequency (density) at which the ARL appears in the plasma is referred to as the continuum threshold frequency (density).

One way in which AWH may be accomplished is when an external antenna is used to excite an eigenmode (typically the first) of the fast magnetoacoustic wave in the vicinity of the ARL. This wave field may undergo the following three types of interactions, depending on the plasma temperature.

(i) If $\omega << k\, v_{te}$, where v_{te} is the electron thermal speed, the fast wave is mode-converted into the kinetic Alfvén wave (KAW) which propagates towards the plasma interior and is damped, owing to the Cerenkov resonance (Landau damping, transit time magnetic pumping, etc.), by the electrons.

(ii) If $\omega \approx k\, v_{te}$ the fast wave is directly damped by the electrons at the resonance due to both the Cerenkov interaction and the plasma resistivity.

(iii) If $\omega >> k\, v_{te}$ the fast wave is mode-converted into the

quasi-electrostatic surface wave which propagates towards the plasma boundary and is weakly damped due to resisitivity.

In all these cases the resulting plasma heating is predicted to be quite local.

AWH is brought about by excitation of a phased array of antennas external to the plasma. In the cylindrical approximation of a tokamak plasma (large aspect ratio limit), the spectrum of waves excited by the antenna consists of eigenfunctions of the form $f(r) \bullet \exp i(nz/R_0 + m\Theta - \omega t)$, where n is the toroidal mode number, m is the poloidal mode number and R_0 is the major radius.

In NET the condition $\omega/\omega_{ci}<<1$ is satisfied for all plasma species and the position of the ARL is given by the simplified expression $\omega=k_{||}(r)C_A(r)$. In this large aspect ratio limit

$$k_{||}(r) = (n+m/q(r))/R_0 \qquad (2.2)$$

where q(r) is the local safety factor.

AWH has the important property that in the cold plasma limit the antenna loading is independent of the damping mechanism, provided the AW fields are localized around the ARL. This remains true in the more general case where kinetic effects are included, provided the KAW is damped before arriving back at the ARL after reflection at the plasma centre. This condition is met for the NET plasma for ARLs at radii greater than about one fifth of the plasma minor radius. In this case the antenna loading is the same in both cold MHD and kinetic theory.

In devices of small dimensions, such as TCA, AWH at low frequency occurs by coupling of the surface branch of the fast magnetoacoustic wave to the AW in the region of the ARL. In large devices, such as NET, coupling to fast magnetoacoustic body waves can occur. These waves, like waveguide electromagnetic waves, only propagate above a cutoff frequency and exhibit strong resonances. As a result, enhanced energy deposition can be expected by exciting the resonances of these waves.

b) The second mode of AWH is where the antenna excites a global eigenmode of the Alfvén wave, or ion cyclotron wave, henceforth referred to as the discrete Alfvén wave (DAW). Since such a mode cannot meet the condition for the spatial Alfvén resonance, its energy is directly dissipated via electron Landau damping and transit time magnetic pumping. In this case the resulting plasma heating has a global character. When $\omega << \omega_{ci}$ the DAW owes its existence to finite plasma current and appears in the cylindrical geometry provided the condition $nq/m > 0$ is satisfied. In a cold plasma, a DAW resonance of a given mode (n,m) appears just below the threshold of the corresponding continuum. In a hot plasma these resonances correspond to standing KAWs.

The development of theoretical work related to Alfvén Wave Heating began as early as 1965-66 in pioneering papers by Dolgopolov and Stepanov [1,2]. Using a simple model they showed that the collisional or Landau damping of the fast magnetoacoustic wave in an inhomogeneous plasma can be strongly enhanced if the condition for the spatial Alfvén resonance is satisfied. The resulting absorbed power was estimated to be of the same order of magnitude as the circulating power. They had thus predicted one of the most typical characteristics of Alfvén Wave Heating.

Up to the present the number of theoretical papers on the subject in question has reached about 120. In this report it is impossible to give a full account of all of them. We shall therefore confine ourselves to a brief chronological list of those which we consider to be the highlights.

Alfvén Wave Heating as a scheme for heating tokamak plasmas was first proposed in 1973-74 independently by Tataronis and Grossmann [3], and by Hasegawa and Chen [4,5]. An important result of the latter authors, obtained using an MHD model in a slab geometry, was that the absorbed power is strongly enhanced if the surface mode (the first radial eigenmode of the fast magnetoacoustic wave) is excited in the plasma. Later, it was shown by the same authors [6,7], using a simple kinetic model in a slab geometry, that in a hot plasma the fast magnetoacoustic wave is mode-converted into the kinetic Alfvén wave in the neighbourhood of the spatial Alfvén resonance. The amount of absorbed power was found to be the same as that obtained from the MHD calculations. The first numerical calculations based on the MHD equations in a cylindrical geometry were

carried out in 1976 [8]. The authors confirmed the importance of the excitation of the surface mode. More detailed numerical computations [9], using the same model, revealed that the presence of an equilibrium plasma current can dramatically improve the coupling to the innermost resonance surfaces. The phenomenon was later identified [10] as being due to the effects of magnetic field curvature.

The first calculations based on the MHD equations in toroidal geometry were performed in 1980 by the Lausanne group [11,12]. It was found that for a circular cross-section the overall coupling is much the same as that obtained from the cylindrical model, except for some additional resonance surfaces which are excited due to interaction between different poloidal modes. Some additional differences are found for non-circular cross-sections, due to ellipticity, triangularity, etc.

The existence of global eigenmodes of the Alfvén wave in the cylindrical MHD model was shown for the first time in 1982 [13,14]. It was shown that their frequencies lie just below the lower edge of the Alfvén continuum (the lowest frequency for which there is an Alfvén resonance layer in the plasma) and that they are "generated" by the curvature of the equilibrium magnetic field lines. In the same year their existence was also confirmed in cylindrical kinetic calculations [15] which took into account the effects of finite ion Larmor radius and parallel electron dynamics (Landau damping). The results also indicated that quasi-electrostatic surface waves could be excited near the plasma periphery.

The importance of including finite ω/ω_{ci}, which arises by including the Hall term in Ohm's law, was pointed out for the first time in 1983 [16]. It was shown that this strongly modifies the coupling of the modes with $m<0$, m being the poloidal wavenumber. A more detailed picture of the influence of finite frequency effects on the spectrum of a cylindrical cold plasma was obtained in [17,18]. In 1985-86 these effects were included in the toroidal numerical code LION [19-21].

Finally, rather general expressions for the dielectric tensor operator of a hot plasma in slab and cylindrical geometries have been derived [22,23] and an appropriate local power absorption formulated [24]. They have been incorporated into different versions of the numerical code

ISMENE [25].

2.2 Current Theory

The present state of affairs can be summarized as follows. The most advanced tools for the theoretical modelling of Alfvén Wave Heating are cylindrical kinetic codes: Sydney [27], Lausanne [23], Sukhumi [26] and Austin [28]. The most developed is the Lausanne code: it takes into account finite frequency effects, Larmor radius terms up to the second order, the gradients of equilibrium quantities, an equilibrium current, Landau damping, transit time magnetic pumping and resistivity. It allows computation of all variable field components, the perturbed electron density, the total power delivered by an antenna and the local power deposition profile. On the other hand, the codes which treat a tokamak in toroidal geometry are less advanced. The most developed is LION [21], which is based on a cold plasma model taking into account finite frequency effects and an equilibrium current. It can only be used, however, to calculate the total power delivered by an antenna. Thus, what is missing at present is a toroidal kinetic code.

References

[1] V.V. Dolgopolov and K.N. Stepanov, Nucl. Fusion 5 (1965) 276.

[2] V.V. Dolgopolov and K.N. Stepanov, Zh. Tekh. Fiz. 36 (1966)1003. [Sov. Phys. Tech. Phys. 11 (1966) 741].

[3] J.A. Tataronis and W. Grossmann, Z. Phys. 261 (1973) 203, 217.

[4] A. Hasegawa and L. Chen, Phys. Rev. Lett. 32 (1974) 454.

[5] L. Chen and A. Hasegawa, Phys. Fluids 17 (1974) 1399.

[6] A. Hasegawa and L. Chen, Phys. Rev. Lett. 35 (1975) 370.

[7] A. Hasegawa and L. Chen, Phys. Fluids 19 (1976) 1924.

[8] J.A. Tataronis and W. Grossmann, Nucl. Fusion 16 (1976) 667.

[9] K. Appert, B. Balet, R. Gruber, F. Troyon and J. Vaclavik, in Plasma Physics and Controlled Nuclear Fusion Research (Proc. 8th Int. Conf. Brussels, 1980), Vol. 2, IAEA, Vienna (1981) 43.

[10] K. Appert, B. Balet and J. Vaclavik, Phys. Lett. 87A (1982) 233.

[11] K. Appert, B. Balet, R. Gruber, F. Troyon, T. Tsunematsu and J. Vaclavik, in Heating in Toroidal Plasmas (Proc. 2nd Joint Varenna-Grenoble Int. Symp. Como, 1980), Vol. 2 (1980) 643.

[12] K. Appert, B. Balet, R. Gruber, F. Troyon, T. Tsunematsu and J. Vaclavik,

Nucl. Fusion 22 (1982) 903.

[13] K. Appert, R. Gruber, F. Troyon and J. Vaclavik, in Heating in Toroidal Plasmas (Proc. 3rd Joint Varenna-Grenoble Int. Symp. Grenoble, 1982), Vol. 1 (1982) 203.

[14] K. Appert, R. Gruber, F. Troyon and J. Vaclavik, Plasma Phys. 24 (1982) 1147.

[15] D.W. Ross, G.L. Chen and S.M. Mahajan, Phys. Fluids 25 (1982) 652.

[16] K. Appert and J. Vaclavik, Plasma Phys. 25 (1983) 551.

[17] G.A. Collins, N.F. Cramer and I.J. Donnelly, Plasma Phys. Control Fusion 26 (1984) 273.

[18] K. Appert, J. Vaclavik and L. Villard, Phys. Fluids 27 (1984) 432.

[19] K. Appert, G.A. Collins, F. Hofmann, R. Keller, A. Lietti, J.B. Lister, A. Pochelon and L. Villard, Phys. Rev. Lett 54 (1985) 1671.

[20] K. Appert, G.A. Collins, T. Hellsten, J. Vaclavik and L. Villard, Plasma Phys. Control. Fusion 28 (1986) 133.

[21] L. Villard, K. Appert, R. Gruber and J. Vaclavik, Comput. Phys, Reports 4 (1986) 95.

[22] Th. Martin and J. Vaclavik, Helv. Phys. Acta 60 (1987) 471.

[23] K. Appert, T. Hellsten, H. Lütjens, O. Sauter, J. Vaclavik and L. Villard, in Proc. 7th Int. Conf. on Plasma Physics, Kiev, Invited Papers, Vol. 2 (1987) 1230.

[24] J. Vaclavik and K. Appert, Plasma Phys. Control. Fusion 29 (1987) 257.

[25] K. Appert, T. Hellsten, J. Vaclavik and L. Villard, Comp. Phys. Comm. 40 (1986) 73.

[26] A.G. Kirov, V.P. Sidorov, S.N. Lozovskij, A.G. Elfimov, L.F. Ruchko, K.G. Komoshvili and V.V. Dorokhov, in Controlled Fusion and Plasma Physics (Proc. 12th Europ. Conf. Budapest, 1985), Vol. 9F, Part 2 (1985) 260.

[27] I.J. Donnelly, B.E. Clancy and N.F. Cramer, J. Plasma Phys. 35 (1986) 75.

[28] Y.M. Li, S.M. Mahajan and D.W. Ross, Phys. Fluids 30 (1987) 2101.

[29] K. Appert, G. Besson, G.G. Borg, B.P. Duval, A.A. Howling, B. Joye, J.B. Lister, J.-M. Moret, F. Ryter, J. Vaclavik and H. Weisen in Proc. 7th Int. Conf. on Plasma Physics, Kiev, Invited Papers (1987).

3. EXPERIMENTAL WORK ON AWH

3.1 Review of Devices

AWH has been experimentally studied on many devices, of which the most important ones are listed in Table 3.1. All are tokamaks, with the exception of R-O, which is included because of its results with current drive. Work has also been carried out on the Wisconsin TOKAPOLE device, which is summarized by Kortbawi [1] as well as the URAGAN device [2]. However the geometry of these machines differs greatly from that of a tokamak and so the applicability of these results to tokamak heating is difficult to assess. Since the greatest volume and variety of work has been carried out on the TCA tokamak, with better diagnosed plasmas and with greater RF power than the remainder, the experimental summary deals mostly with TCA, even if one of the remaining experiments has made similar observations.

TABLE 3.1

Device Parameters

Device:	**TCA**	**TORTUS**	**PRETEXT**	**R-05**	**R-0**
R(m)	0.61	0.44	0.53	0.65	.50
a(m)	0.18	0.10	0.17	0.085	.05
B_T(T)	1.6	1.0	0.80	1.0	0.8
I_p(kA)	170	30.0	35	10	-
$n_e(10^{19}m^{-3})$	10	1	2	2	10
T_e(eV)	800	100	200	100	40
Antenna type	poloidal	poloidal	toroidal	helices	helix/ poloidal
Antennae	8	2	2	n=6, m=2	n=2,m=2
RF power (MW)	.6	.06	0.1	-	-
Travelling wave	possible	no	no	yes	yes
Operational	yes	yes	no	?	?
f_o (MHz)	2.5	1-20	2.1	3	1.3-2.2
Reference	Cheetham [3]	Brennan [4]	Evans [5]	Demirkhanov [6]	Demirkhanov [7]

3.1.1 TCA

TCA is equipped with 8 groups of unshielded antennae, each one comprising 6 parallel bars in the poloidal direction. The bars are each 10mm in diameter and coated with 6-7μm of TiN. The RF current can be reversed in any group by reconnecting. The current can be more finely dephased when needed, up to $\pm\pi/4$ per group. The present RF generator is described in detail by LIETTI and BESSON [8] and can deliver 1.6 MW into a dummy load. The pulse length can be up to 200 msec, greater than the TCA flat-top (170msec). As well as giving amplitude control, the RF generator can also be swept in frequency, but losing delivered power as the antenna matching circuit is detuned. The available frequency range corresponds to ±10%.

3.1.2 TORTUS

The TORTUS tokamak is presently fitted with 2 antennae, giving up to 30 kW of RF power each. The antennae are fully shielded, as described by BRENNAN et al. [7]. Work has also been carried out using a rotatable antenna, described in detail by BORG et al., [9]. Operation is limited in density and current range. However a large (1 - 20 MHz) operating frequency range is possible.

3.1.3. PRETEXT

The PRETEXT tokamak is no longer operational. Work was mainly devoted to studying the synchronous density modulation (EVANS, [5] 198-PRL). The antennae were originally toroidal bars, but were later replaced by poloidal structures, as on TCA.

3.1.4. R-05

The R-05 Tokamak has apparently suffered technical difficulties not associated with the RF heating, delaying its first RF results. The antenna structure is helicoidal outside a ceramic vacuum vessel [6] . The RF system installed is extremely high powered but for only a short RF pulse duration, of the order of a few msec.

3.1.5. R-0

R-0 is a stellarator (l=3) in which RF power was used to create and heat the plasma, as well as to drive plasma current. Since there was no tokamak-type induced current, they were able to detect a small RF-driven

current. The antennae were helicoidal and poloidal, outside a ceramic vessel. The RF pulse lasted for 2 msec.

3.1.6. ASDEX

An experiment is being commissioned on ASDEX to explore AWH at modest RF power (of the order of the ohmic power) using only two antennae mounted poloidally on the mid-plane.

3.2 Review of AWH Experimental Results

3.2.1. Wave launching

The launching of Alfvén Waves in TCA is studied using the individual antenna loading resistance (defined such that $P_{RF} = 1/2\ I^2_{ant}R_{ant}$ for each antenna), the RF wavefield amplitudes and the driven density oscillations. The antenna loading curves, as a function of the spectral parameter $f^2ne = (n+m/q(r))^2 \times B_\phi{}^2/(\mu_0\rho(r)/n_e \bullet 4\pi^2R^2)$, show the presence of both continuum and eigenmode loadings. These results are described in detail by COLLINS et al. [10], showing that the toroidicity and finite frequency effects must be taken into consideration. The same reference describes the RF wavefield measurements and the observation of driven travelling waves.

Finite frequency effects and the dependence of the parasitic edge loading on the angle of the antenna bars to the toroidal axis were investigated by BORG et al. [9]. Travelling waves were generated in the R-0 stellarator, and the measured wavefields agreed with the predictions of KIROV et al., [11]. Detailed probe measurements have also been made in the PRETEXT tokamak.

The density fluctuations associated with the RF wave were observed on PRETEXT [5] for a particular eigenmode, but not for the continuum. Both the continuum and eigenmode fluctuations have been observed on TCA [12], confirming the density dependence of the radius of the continuum resonant layers. Although the presence of density fluctuations confirm the importance of kinetic effects ($T_e>0$), antenna loading and wavefield measurements, performed by (APPERT et al., [13], also show details which had been predicted by kinetic theory.

The results of experiments on the launching of Alfvén waves support the large volume of theory previously developed. We have little reason to doubt the validity of the current models, although calculations in toroidal geometry with a hot plasma model have yet to be performed.

3.2.2. Electron Heating

On TCA a large increase in the electron temperature sawtooth slope has been observed during AWH [14]. The increase in the mean temperature on axis of several hundred eV is not maintained throughout the RF pulse [15] due to the increase in electron density (3.2.4.). Present results indicate that the RF power is absorbed mostly by the electrons. Power modulation experiments [16] indicate a strong dependence on the plasma current and an inexplicably large phase delay. The mechanisms underlying these phenomena are not yet fully understood. Recently it has been suggested [16] that a large fraction of this apparently strong heating may be an indirect result of the density change. It is difficult to estimate any change in confinement time because of the electron density increase and the lack of a steady state.

3.2.3. Ion Heating

The ion temperature increases by several hundred electron volts during the RF pulse. This increase is due mostly to the increase in collisional power transfer when the density rises. However, a part of the increase must be attributed to an RF-related effect. Possibilities are an increase in effective collisionality, a decrease in diffusion or a direct heating [17].

3.2.4. Density Rise

A density rise has always been observed on TCA during the RF pulse. The origin of this has not been identified, even though the magnitude of the effect is important; tripling the target density in extreme cases. The density during the RF pulse has not yet exceeded the ohmic limit. Experiments using lateral screens failed to reduce the rise, although TORTUS has shown that a full screen can inhibit the density rise at low power [4]. The density rise in TCA exhibits discontinuous behaviour when the excited spectrum changes, suggesting an internal mechanism, or at least one related to the RF wave. Measurements taken on R-0 have shown that the details of the structure of travelling waves alter the density

profile considerably. A decrease in the H_α emission compared to the ohmic value suggests a possible change in particle confinement [18].

3.2.5 Increase in $(\beta+l_i/2)$

The quantity $(\beta+l_i/2)$ increases considerably during AWH, up to a factor of 1.55 at low current [13]. This increase is partly due to an increase in β during the density rise, but also due to an increase in l_i. The increase is largest for the more "inefficient" resonance layers near the edge of the plasma, suggesting that these outer layers effect the current profile. The dependence of the $(\beta+l_i/2)$ increase on the plasma current leads us to define the quantity $(\beta+l_i/2\text{-}0.7)\ I_p$, which has an upper experimental limit. This result is also not fully understood.

3.2.6 MHD activity

The changes in MHD activity (m=2, Mirnov) observed on TCA are linked to the excited spectrum [13]. Ultimately the plasma disrupts at high power, when the m=2 activity reaches a sufficiently high level. This level can, in fact, be predicted from low power measurements by following the m=2 development. Our delivered power has been limited to 570 kW due to such disruptions. The sensitivity to the spectrum is linked to the change in l_i previously mentioned, which also occurs when the excited spectrum changes. It is not clear why the m=2 driven disruption corresponds to a given value of $(\beta+l_i/2\ -0.7)I_p$.

3.2.7. Summary

This outline of the experimental results can be summarized as follows:

- The wave launching is very well documented and agrees with theory when toroidicity, plasma current, finite frequency and finite temperature are considered.
- Significant increases in the energy content of the plasma confirm the energy transfer and dissipation processes within the plasma.
- The RF power has other dramatic effects on the plasma which may be linked to changes in the current profile.
- The density rise makes the energy balance difficult to analyse.

3.3 Future Work

Future work on TCA includes:

- addition of full quartz screens to investigate the density rise,
- use of higher frequencies and larger values of ω/ω_{ci},
- installation of tilted antennae.

Apart from TCA, results are still expected from the ASDEX experiment and TORTUS will continue to provide data on the wave launching mechanisms.

3.4 Outstanding Questions

The following represent the major outstanding issues which must be addressed :

- The confirmation of the effect of the outer resonance layers.
- The explanation of the limit of $(\beta+l_i/2)$ observed on TCA.
- The explanation or control of the density rise.

References

[1] D. Kortbawi, Ph. D., Thesis, University of Wisconsin (1987).
[2] O.M. Shvets et al., in Proc. 4th Int. Symposium on Heating in Toroidal Plasmas, Vol. 1 (1984) 513.
[3] A.D. Cheetham et al. in Proc. 11th Symp. of Fusion Technology, Oxford, Vol. 1 (1980) 601.
[4] M.H. Brennan et al., Proc. 29th Int. Conf. APS, San Diego (1987).
[5] Evans et al., Phys. Rev. Lett. 53 (1984) 1743.
[6] Demirkhanov et al., Zh. Eksp. Teor. Fiz. 33 (1981) 31.
[7] Demirkhanov (1980).
[8] A. Lietti and G. Besson, J. Phys. E, 19, (1986) 110.
[9] G.G. Borg et al., Proc. 13th Europ. Conf. on Contr. Fus. and Plasma Heating, Schliersee, Vol. 10c, part II (1986) 52.
[10] G.A. Collins et al., Phys. Fluids 29 (1986) 2260.
[11] G.A. Kirov et al., Plas. Phys. and Contr. Nuc. Fus. Res. (1984).
[12] R. Behn et al., Plas. Phys. and Contr. Fus., 29 (1987) 75.
[13] K. Appert et al. in Proc. 7th Int. Conf. on Plasma Physics, Kiev, Invited Papers, Vol. 10 (1987) 550.

[14] B. Joye et al., Phys. Rev. Lett. 56 (1986) 2481.
[15] G. Besson et al., Plas. Phys. and Contr. Fus. 28 (1986) 1291.
[16] B. Joye et al., Plas. Phys. and Contr. Fus. submitted for publication.
[17] A. de Chambrier, Ph.D. Thesis, Lausanne (1988).
[18] R. Behn et al., Plas. Phys. and Contr. Fus. 26 (1984) 173.

4. APPLICATION OF AWH TO NET

4.1 Introduction

The interest of Alfvén Wave Heating to NET resides in the conceptual difficulty in optimising the NET plasma itself. For this reason, any additional method of plasma heating or current profile control could be useful because of the changes it brings about in a tokamak plasma. We consider that the experimental results obtained on TCA are of primary interest due to the changes in the plasma parameters (density rise, $\beta+l_i/2$ increase and spectral dependence) rather than any results indicating that it is a superior method of substantially increasing the energy content.

Nevertheless the low frequencies used in Alfvén wave heating could lead to certain advantages, namely:

i) The frequencies used (a few megahertz) is within the range of existing, well-established technology. Conventional power generation and transport techniques could be used at the levels required for NET.

ii) Existing high-power tubes lead to a design with relatively high unit output power.

iii) As the technology is already established, the cost per delivered MW is relatively low.

iv) The simple technology, both inside and outside the torus, would facilitate the design and construction of the AWH system.

Some of these points are treated in Chapter 7, together with the in-torus antenna itself.

4.2 Plasma Heating

The current experimental results were summarized in Section 3.3. The fundamental requirement for NET will be to increase the ion temperature of a collisional plasma, more typical of older experiments than the less collisional JET heated plasmas. The ion heating results on TCA must be

interpreted with care since the conditions correspond to $n_e = 6x10^{19}m^{-3}$, $T_e = 1$ keV, 12 times more collisional than NET at $n_e = 10^{20}m^{-3}$, $T_e = 10$ keV. No steady-state data has been obtained on TCA for which the ion temperature was greater than the maximum ohmically heated value, although the ion temperature at a given density is higher during AWH than in purely ohmically heated plasmas at the same density. Despite considerable success in understanding the physics of Alfvén wave heating, it would still be premature to consider it proven to the extend required to adopt the concept in NET.

4.3 Current Drive

It has been realised that since Alfvén waves can be driven in the toroidal direction, and that dissipation of the wave momentum is parallel to the toroidal axis, current drive should be feasible. Working against this is the damping of a toroidally slow part of the electron distribution, resulting in this fraction being toroidally trapped.

At present, the TCA experiment has shown no definitive driven current. R-O remains the only machine exhibiting significant plasma current driven by travelling Alfvén waves.

4.4 Operational Range

The main advantage of AWH is its relative insensitivity to the plasma parameters. Nothing in the present theory of AWH suggests any form of density cut-off, magnetic field or size limitation. In addition, no scrape-off propagation is needed to launch the surface waves. The question of range coverage is addressed in Chapter 8.

4.5 Antennae

AWH is often considered impractical due to the requirement of an internal antenna structure. In Chapter 7 we shall see that a recessed antenna should be compatible with the antenna loading requirements.

4.6 Subsequent Programme

The inadequate experimental results of the heating scheme, together with the somewhat perplexing initial results from ASDEX, are despite our apparently good understanding of the wave coupling mechanisms. The risk at present is that an important factor is missing in our understanding of AWH, such as an unidentified competing dissipation channel for the driven waves. Since the driven waves are global, in the sense that they are toroidally uniform and have a significant wavefield over the whole torus volume, many such competing mechanisms must be considered.

This question must be addressed on TCA. The present ASDEX pilot study is limited in duration. After its closure only TCA and TORTUS will be active in AWH research. Such an approach is inadequate to prove applicability in NET. In May 1988 these problems are unresolved, and despite the good physics base, the technological attractiveness and the operational flexibility, AWH remains unproven.

5. EXTRAPOLATION OF THE PHYSICS OF AWH TO NET

5.1. Introduction

In this chapter we consider the physics of AWH in a fusion plasma and the scaling of the antenna loading from a small experimental device, TCA, to a NET equivalent. A set of scaling laws valid in the ideal MHD limit will be presented, which allow the AWH antenna loading to be scaled with frequency and dimensions in a fixed geometry.

The general validity of the theory of AWH and, to a lesser extent, the scaling laws have already been verified in the experiments conducted during the past eight years on the TCA tokamak.

The study presented in this chapter has required the use of several techniques of analysis. These are now briefly described.

An approximate analytical expression is derived for the Alfvén Wave loading due to an antenna external to a slab plasma in the ideal MHD limit. The expression is an approximate solution to the governing equations and does not accurately predict the antenna loading. Although the scaling laws of loading in AWH are well known, they are not conveniently available. The purpose of the analytical expression is therefore pedagogic. It does, however, describe the effect of changing the distance from wall to antenna and antenna to plasma.

Although the general validity of the ideal MHD scaling laws will be established for a range of plasma parameters between TCA and NET, this validity is not at all evident a priori. A more detailed calculation is therefore needed to include non-ideal MHD effects; finite frequency, finite electron mass, finite plasma current and kinetic effects. To this end, calculations will be based on the 1D kinetic code ISMENE previously mentioned.

We wish to model a travelling wave poloidal antenna with radial feeders. The poloidal component consists of currents of the form:

$$j_\Theta = k_z \beta_o \delta (r - R_A) \qquad (5.1)$$

where k_z is the toroidal wave number and R_A is the antenna radius. The antenna loading (R_{ant}) to be quoted from the 1D kinetic code is caclulated assuming that the equivalent current flowing in the antenna is given by $2\beta_o$.

5.2 Scaling of AWH to Reactor Conditions

Although codes include much of the known physics they are normally restricted to simplified geometries. In particular, ISMENE does not include effects due to toroidicity, non circularity, the near fields of a conducting antenna or toroidal and poloidal boundary inhomogeneities such as wall recesses. The result is that codes do not provide accurate predictions of antenna loading. If, on the other hand, a set of scaling laws can be established within the limitations of the wave physics, the known experimental results can be scaled from small tokamaks to reactor tokamaks in order to predict the actual antenna loading and plasma heating. Although such extrapolations are restricted to configurations of identical geometry, the values obtained are good 'ball-park' estimates for similar sized configurations of differing geometry.

In this section, we develop the scaling laws for the antenna loading from first principles in the ideal MHD limit. These laws are applied at a fixed point in the spectrum. This means that the parameters ω, B, n_e, R_0 and I_p in equations 2.1 and 2.2 are always varied in such a way that the ARL radius remains at a fixed fraction of the minor radius R_p.

These scaling laws are checked for a range of plasma parameters (including those of NET) using the cylindrical code ISMENE. To this end we adopt the following NET equivalent cylindrical parameters based on the NET double null configuration [1].

Plasma Major Radius	R_0	5.18 m
Plasma Minor Radius	R_p	2.17 m
Antenna Radius	R_A	2.28 m
Wall Radius	R_W	2.39 m
Plasma Current	I_p	10.8 MA
Plasma Current Density Profile		$(1-(r/R_p)^2)^2$

Toroidal Field	B	5 T
Safety Factor at Edge	$q(R_p)$	2.1
Electron Density on Axis	$n_e(0)$	$17.9 \times 10^{19} m^{-3}$
Electron Density Profile		$1-0.99(r/R_p)^2$
Ion, Electron Temperature on axis	$T_{i,e}(0)$	14.9 keV
Temperature profile		$1-0.99(r/R_p)^2$
Ratio of D to T		1.0
$\omega_{ci}(min)$		25 MHz

Unless otherwise stated the primary fixed parameter in all numerical results to be presented is the radial position of the ARL. In order that the power deposition be fairly central and that the following study be a typical case for the AWH schemes presented in Chapter 8, the ARL has been fixed at the half central density point. For a parabolic density profile, with a $0.01 n_e(0)$ density pedestal at the plasma edge, the ARL is situated at radius of 0.71 R_p. The scaling laws will be checked for wave modes with $|m|=1$ since it is this mode which is most efficiently coupled.

5.2.1 Antenna loading in an ideal MHD slab plasma

Consider the slab plasma depicted in Fig. 5.1, with a uniform magnetic field in the z-direction, a linear density profile for $x \geq 0$ and a vacuum layer for $-h_2 < x < 0$. Let the antenna current be specified by:

$$J = \Lambda_0 \delta (x + h_1) \exp i(k_y y + k_z z - \omega t)$$

where Λ_0 is the current per unit width, k_y and k_z are the wave numbers and ω is the operating frequency. If one assumes that $k_y >> k_z$, $k_y h_2 << 1$ and that the ARL lies within the plasma at x_0 so that $\omega = k_z V_A(x_0)$ is satisfied, then the power P delivered to the plasma in the ideal MHD limit is given by:

$$P = \frac{\pi \omega \mu_o \Lambda_o^2}{2x_o} \frac{L_z L_y (h_1 - h_2)^2}{K_o^2(k_y x_o) + \pi^2 I_o^2(k_y x_o)} \qquad (5.2)$$

where L_y and L_z are the plasma dimensions in the y and z directions and K_0

and I_0 are modified Bessel functions. This formula corresponds to that of Hasegawa and Chen [2] except that in their model $h_2 = -\infty$ and a constant density was assumed at some value $x > x_0$. It should be noted from equation (5.1) that whenever a scaling involves a change in R_p, R_0 or B, then I_p has to be changed to keep $q(x_0)$ and hence x_0 constant.

5.2.2 Scaling of antenna loading with frequency

According to equation (5.2), if the spectrum, the ARL position x_0, the wave numbers and the geometry are held fixed, then the loading scales linearly with frequency, ω. In this case x_0 is held constant as the frequency is changed by modifying either B or n_e as previously mentioned. Similarly, if ω is fixed and B and n_e are changed such that x_0 remains constant, then the loading should remain constant.

This frequency scaling was tested for NET conditions using the code for the 32 combinations of modes, $|m| = 1$ and $|n| = 1,2,4,8$, for densities from $n_e = 0.01 \times 10^{19}$ m^{-3} to 100×10^{19} m^{-3} and for B = 1T and 5T. The results shown in Fig. 5.2 for m = -1, n = -1, -2, -4, -8 indicate that the ideal MHD scaling is valid (i.e. R/ω independent of frequency) provided that $n_e > 1.0 \times 10^{19}$ m^{-3}, which is the case in TCA and would be the case in NET. At low densities the comparison is invalid due to both finite frequency and electron mass effects.

In conclusion it may be stated that the $R_{ant} \sim \omega$ scaling applies in the rectangle of parameter space defined by $1 < B < 5$T and $1.0 < n_e < 100 \times 10^{19}$m^{-3}.

5.2.3 Scaling of loading with antenna-wall spacing

From Equation (5.2) it is immediately evident that the loading increases quadratically with the distance between the antenna and the wall provided that $k_y h_1 << 1$. In addition, the loading is independent of the distance h_2 from the plasma to the antenna when $k_y h_2 << 1$. This result has been previously observed in antenna optimisation calculations for TCA [3] and has now been confirmed by the code (Fig. 5.3.) for all combinations of mode numbers tried. Its immediate application is that the antenna can be withdrawn from the plasma for protection from plasma particle interaction but it should be kept as far as possible from the wall to avoid

close image currents. The effect of the wall is further treated in Chapter 7, where the effects of a recess are taken into account. The validity of the quadratic scaling independent of toroidal mode number n implies that the total antenna loading can be scaled once it is known for one antenna-wall separation.

5.2.4 Scaling with vessel size

If the geometry and spectrum are held fixed then the antenna loading scales with the major radius (note that Λ_0 in equation (5.2) is the current per unit width in the antenna). The particular scaling chosen is ω, B constant; $n_e \sim I/R_0^2$; $R_p \sim R_0$; $I_p \sim R_0$ and $T_{i,e} \sim R_p^2$.

Although the temperature $T_{i,e}$ does not explicitly enter the MHD scaling, a temperature scaling has been adopted to keep the wavelength and damping [3] of the KAW constant.

The results shown in Fig. 5.4. were calculated for $|m|=1$ and $|n|=1,2,4$ and 8. A known antenna loading in ASDEX can be extrapolated to a NET loading with a 20% error bar. It should be noted, however, that a choice of scaling in which ω/ω_{ci} is not fixed could break down at small major radii.

5.2.5 Scaling from TCA to NET

The scalings of Alfvén loading with frequency (Section 5.2.2) and with vessel size (Section 5.2.4.) will now be used to predict the Alfvén loading in a large tokamak with the NET major radius by a direct scaling of the TCA experimental loading. It should be mentioned that, because TCA and NET have different aspect ratios, it is not possible to scale to a reactor with the precise parameters cited in Section 5.1. The new scaled reactor "TCA-NET" parameters compare with the TCA parameters as follows:

		TCA	TCA-NET
R_0	(m)	0.61	5.18
R_p	(m)	0.18	1.53
B	(T)	1.51	5
I_p	(kA)	130	3,640
freq	(MHz)	2.5	0.50
$q(R_p)$		3.1	3.1
$n_e(0)(x10^{19}m^{-3})$		1.5 - 9.8	5.7 - 37.0

where the density range chosen corresponds to a scan of the |n|=2, |m|=1 spectrum in TCA.

Since the "TCA-NET" parameters have been chosen to keep a fixed point in the spectrum, the "TCA-NET" loading is obtained from the TCA loading simply by scaling up in proportion to frequency and major radius.

As an example, we consider the TCA experimental loading per antenna (Fig. 8 in [5]) reproduced in Fig. 5.5. The TCA antenna was phased to excite |n|=2 and |m|=1. The large central peak in the trace is the (-2,-1) Discrete Alfvén Wave (DAW). In addition, we know that there is also a (2,1) DAW of much lower amplitude, not evident in the experimental trace, and a sequence of higher order modes more heavily damped. These |m|=1 DAWs are excited directly by the antenna, and are predicted by the cylindrical code. Also evident in the experimental trace are the (2,0) and (2,2) DAWs, both of which are the result of toroidal coupling [7], and are therefore not predicted by the cylindrical kinetic code.

The TCA-NET loading is obtained from the TCA loading simply by adjusting the load axis according to the vessel size and frequency scaling. In Fig. 5.5. the TCA load axis is shown on the left and the TCA-NET load axis is shown on the right. It should be noted that the scaling law does not apply to the DAWs, or to the continua, when the ARL is too close to the centre of the plasma.

The loading in the (2,1) continuum for the TCA and TCA-NET plasmas can be calculated by the code using the respective parameters. The total load is obtained by adding the loads for (n,m) = (+2, +1) and (-2, -1); the two modes driving the (2,1) ARL.

The experimental (2,1) continuum loading is obtained by subtracting the (2,0), (2, -1) and (-2, 1) loads; i.e. by subtracting the loading level before the (2,1) DAW. To this end, a load baseline has been drawn on the figure at this level.

In general, it is not possible to compare the code directly with the experimental results because: (a) toroidal effects are not included, (b) the plasma wall distance is not easily estimated if the plasma is circular and

the wall rectangular, and (c) the effects of finite plasma density at the antenna are not included in the code. However, if the ideal MHD limit applies, it will do so regardless of these effects. Hence, scaling of the experimental load when possible, providing it is due to resonant absorption at an ARL, seems to us to be a more reliable means of predicting the antenna load than by running a code.

The results in Fig. 5.5. show good agreement, over the whole density range of the (2,1) continuum, between the scaled experimental results and the code results calculated directly for TCA-NET.

5.3. Summary

Results have been presented which show that scaling laws based on ideal MHD [Equation 5.2] are applicable for the scaling of antenna loading in large tokamaks. A sample scaling from TCA to a NET reactor equivalent shows good agreement with the code and an increase in antenna loading.

References

[1] F. Engelmann, Concept and Parameters of NET, NET report EUR-FU-XII-80/86/84.
[2] A. Hasegawa and L. Chen. Phys. Rev. Lett. 32 (1974) 454.
[3] F. Hofmann et al., Letter in Nuc. Fus., 24 (1984) 1679.
[4] A. Hasegawa and L. Chen, Phys. Rev. Lett. 35 (1975) 370.
[5] G.A. Collins et al., Phys. Fluids 29 (1986) 2260.
[6] K. Appert et al., Phys. Rev. Lett. 54 (1985) 1671.

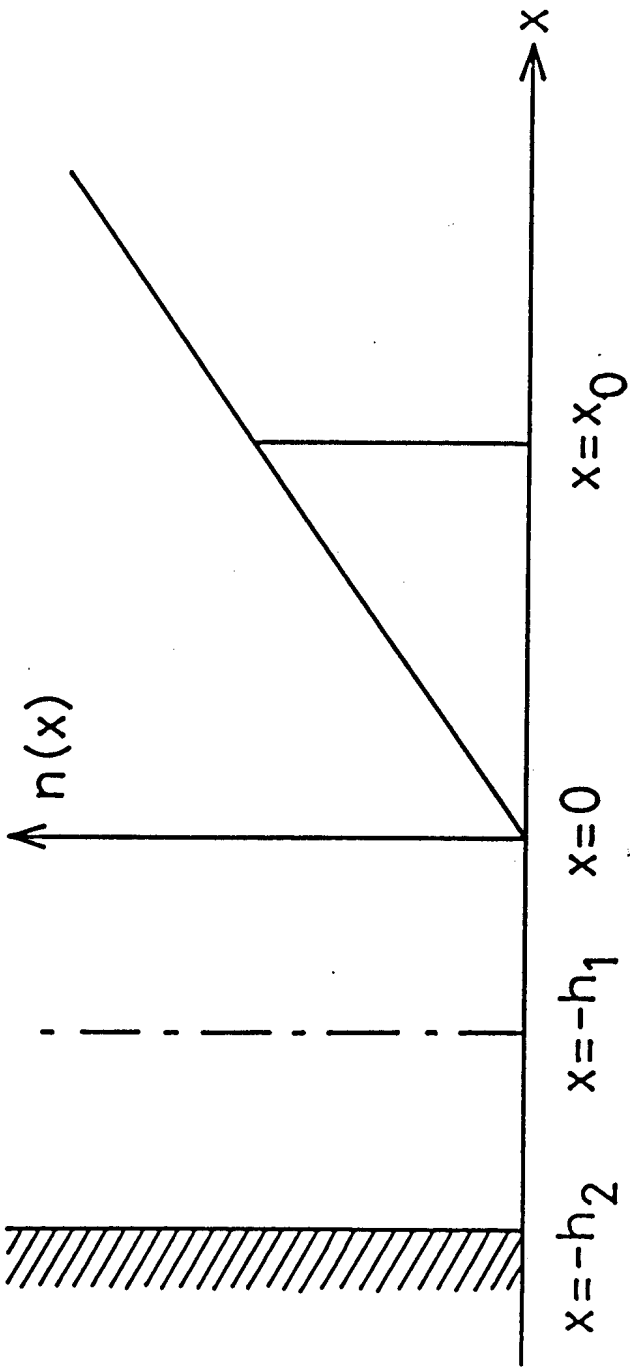

Fig 5.1 Geometry for loading with an ideal MHD slab plasma.

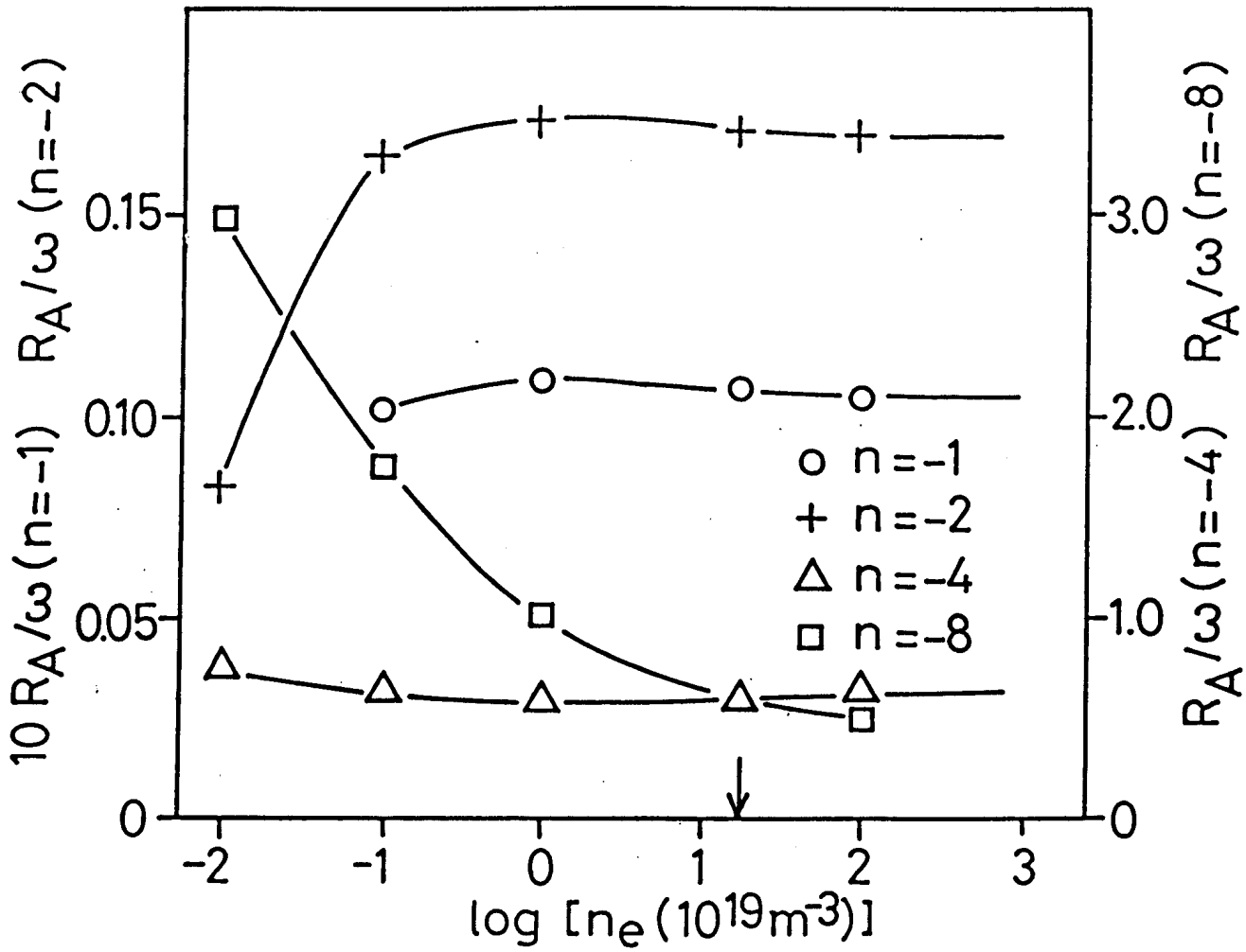

Fig 5.2 Frequency scaling as a function of density with toroidal field equal to 1 and 5 T.

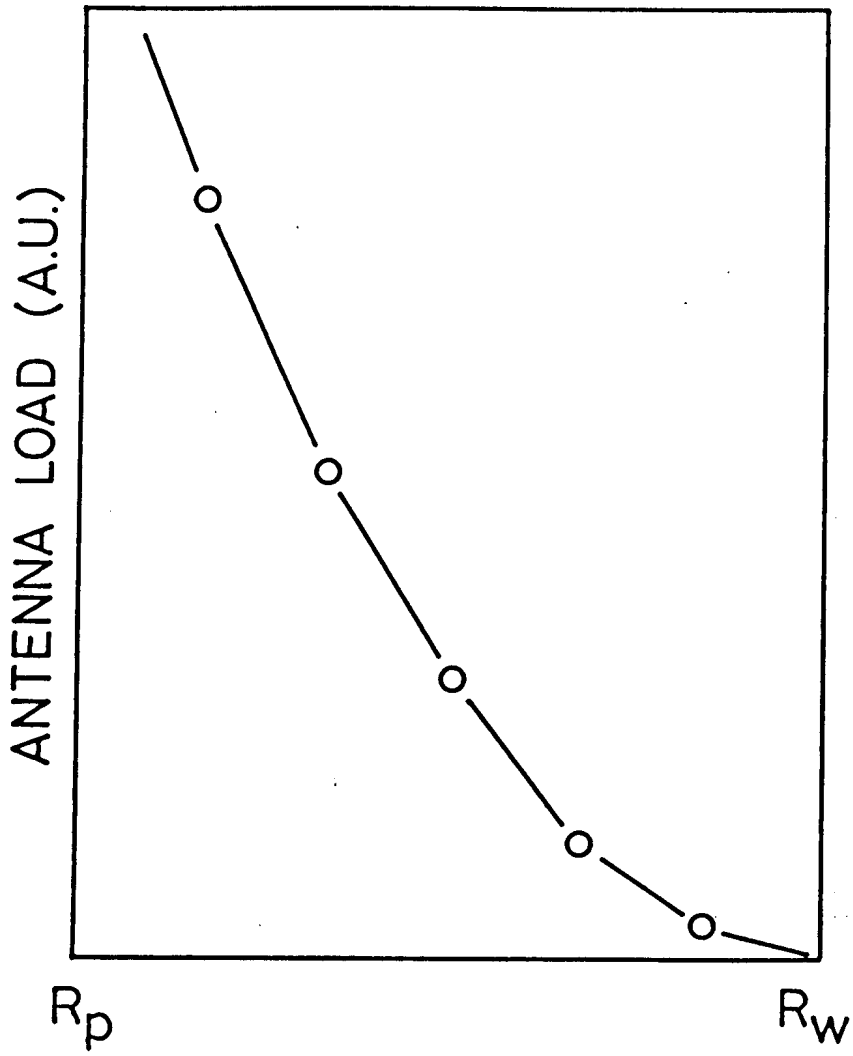

Fig 5.3 Antenna loading as a function of plasma-wall separation.

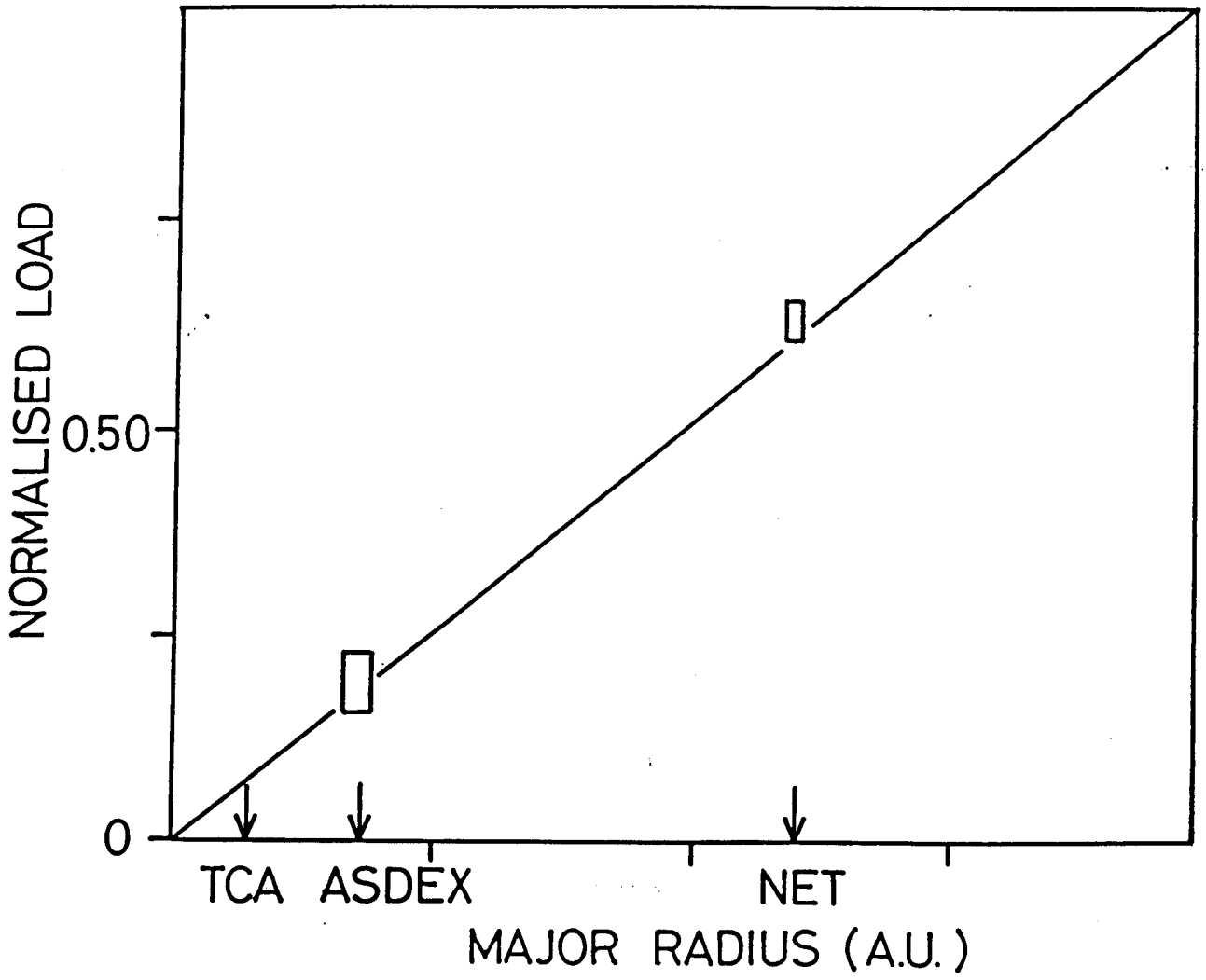

Fig 5.4 Antenna loading scaling as a function of vessel size.

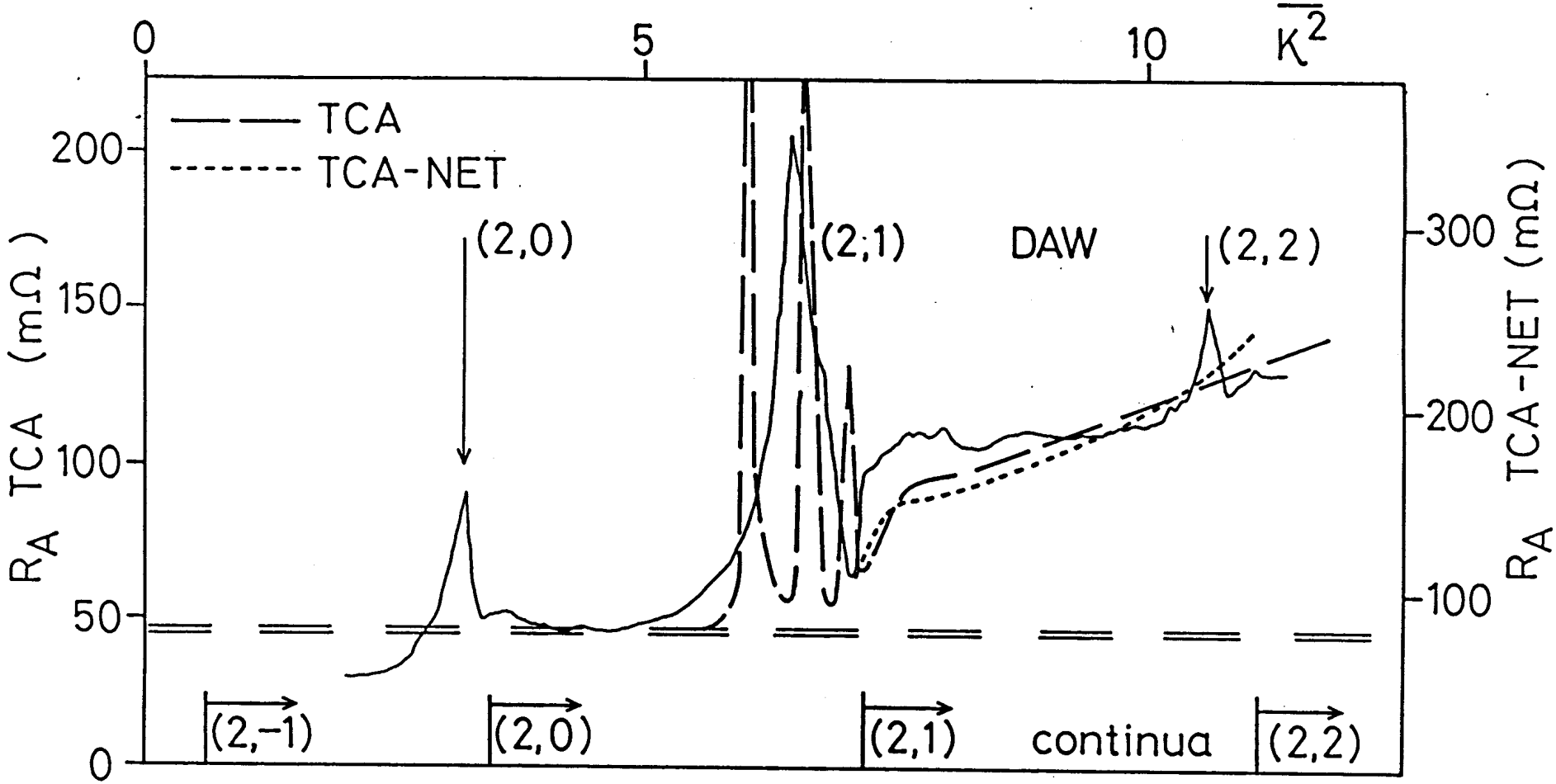

Fig 5.5 Comparison of TCA experimental loading (left axis) with the TCA-NET equivalent scaling (right axis) and the ISMENE calculated loadings.

6. CHOICE OF SUITABLE MODE-NUMBER AND FREQUENCY

6.1 Introduction

An advantage of AWH, arising from the fact that the antennas coherently excite global modes of the torus, is that the loading per antenna element for a given (n,m) mode increases with the number of elements which are phased to favorably excite the mode. For example, a single poloidal antenna element located at a single toroidal location excites a spectrum of modes containing each value of n. An additional element located 180° toroidally and whose current is 180° out of phase suppresses all even modes n=±2, ±4, ±6,... and doubles the loading per antenna element for the odd modes n=±1, ±3, ±5 etc.

In NET, there are 16 oblique and 8 radial access ports, equally spaced in the toroidal direction [1]. An AWH system, which is feasible from the points of view of mechanical simplicity and of power coupling efficiency, can be constructed with modular demountable elements inserted at these ports.

The principal requirement is to maximize the number of antenna elements in order to increase the power input. In addition, since each antenna element must be recessed into the blanket, engineering problems would arise with element arrangements occupying more than one port.

In the following study, therefore, we consider antenna arrangements with either 8 or 16 elements equally spaced in the toroidal direction, and each occupying a single port.

6.2 Operational Frequency Range

A plot of frequency versus the on-axis density which places the ARL at the half density point is shown in Fig. 6.1 for the modes m=0, ±1 and ±3 and n=±1, ±2, ±4, and ±8.

At the NET density, $n_e(0) = 17.9 \times 10^{19} m^{-3}$, the ARL is positioned at the half density point for frequencies below 2.2MHz. This is a very accessible frequency range for high power generators. In practice, when

one operates at a fixed frequency, one must switch excitation mode in order to operate at a central ARL as the density evolves. The subject of mode switching is treated in Chapter 8 where we consider AWH with a typical NET operating scenario.

The loading contours in (ω,n) space for m=1, $|n|>0$ and $n_e(0)=17.9\times10^{19}m^{-3}$ are shown in Fig. 6.2. The solid curves represent the ARLs at $r=R_p$, $0.71R_p$ and $0.9R_p$, and the broken curves are the loading contours obtained directly from the code for the idealized travelling wave antenna. These curves are similar in form to that obtained by APPERT et al. [2] for the case of ideal MHD including plasma current. This is to be expected since the validity of the ideal MHD scaling laws has already been established in Chapter 5. More recently these calculations have been repeated by KIROV et al. [3,4] who have shown that for T-16 and INTOR the optimum n is obtained at $n \bullet R_p/R_0 = 2.5$ or $n \approx 6$ for the case of NET.

As noted by APPERT et al. [2], the existence of such an optimum n is due to the excitation of a weakly damped resonance of the first radial surface wave mode.

The choice of 8 or 16 antenna elements, therefore, strongly favours n=4 to n=8 excitation and, in addition, coincides with the first surface wave resonance.

6.3 The Antenna

The simplest antenna element is the low field side poloidal element (i.e. the antenna current flows in the poloidal plane) presently used in ASDEX and illustrated in Fig. 6.3(a). Starting from this simple concept we consider some alternative element designs and the factors that effect coupling to the ARL, parasitic coupling to the edge plasma and mode number selection.

In the analysis presented in Chapter 5, only $|m|=1$ excitation was considered. The present proposed antenna configuration excites m=0 very strongly. However, both theory and experiment [5] indicate that m=0 coupling is very weak due to the absence of an m=0 surface magnetoacoustic wave branch. Hence there is no advantage, in terms of

spectral purity, in considering an antenna with elements phased 180° out of phase above and below the plasma, as in TCA [5]. If, however, the top and bottom antennas are oppositely phased for $|m|=1$ excitation, then the coherence requires the loading per antenna element to be twice that of the configuration of Fig. 6.3(a). This possibility may be considered as an alternative improved antenna arrangement. It is shown in Fig. 6.3(b).

The coupling of a travelling wave poloidal antenna with feeders in NET does not increase significantly with m for $|m|>1$. Hence there is no need to consider antennas with phased poloidal arrays for excitation of modes with $|m|>1$.

Optimisation of the antennas in Figs. 6.3(a) and (b) requires a choice of the poloidal and toroidal widths of each bar. In general, the loading for high m and n modes decreases as these widths are increased. However, the loading for the lower desired modes also decreases slightly. A discussion of antenna bar dimensions must also include the effects of heating due to the circulating current and will be postponed until Chapter 7.

A larger antenna loading could be achieved by means of a helical antenna. The increased engineering complexity of installing such an antenna cannot be justified, however, for several reasons. The ratio, α, of loading of a travelling wave poloidal antenna with feeders to that of a purely helical antenna [6] is given by:

$$\alpha = ((n/R_0)^2/[(m/R_A)^2 + (n/R_0)^2])^2 \qquad (6.1)$$

This approximate expression gives good agreement with the code for all combinations of the mode numbers. In NET, for $n\geq 4$ the ratio is greater than 50%. Hence for n-modes of interest the poloidal antennas of Figs. 6.3(a) and (b) give almost the same loading as a complete helical antenna. In addition, antennas with current elements directed predominantly along the total steady field have been shown experimentally to have high parasitic loading [7] due to edge plasma dissipation. An optimum configuration appears to be an antenna like that of Fig. 6.3(a) but with elements tilted in the direction normal to the steady field to eliminate parasitic edge dissipation. The antennas of Figs. 6.3(a) and (b) excite equal

amounts of the four sign combinations of n and m. For q>0, the positive helicity modes, (+|n|, +|m|) and (-|n|, -|n|) occupy an inner ARL, and the negative helicity modes (|n|, -|m|) and (-|n|, |n|) occupy an outer ARL, often near the plasma edge. Since typically 50% of the energy deposition occurs in each ARL, significant edge heating is expected to result. If one operates at a low frequency so that the positive helicity ARL is not in the plasma and the negative helicity ARL is centrally positioned, then there is no edge heating; at least for the excited modes. The problem here is that loading is poor at such a low frequency.

A modular helical antenna along the lines of the antenna of Fig. 6.3(a) and show in Fig. 6.3(c) has been proposed [8] for TCA. This antenna has been shown numerically to preferentially excite modes of one helicity for tilt angles much smaller than that of a toroidal helical antenna which excites the same mode. For example, the tilt angle, $d\theta/d\phi$, for (n,m) = (2,1) excitation is 0.2 compared to the helix tilt of 0.5. This allows the antenna elements to be installed in separate ports, as in the case of the antenna of Fig. 6.3(a). The tilt angle for the desired positive helicity mode is such that the antenna currents are more nearly parallel to the steady field than in the case of the purely poloidal antenna of Fig. 6.3(a), thus leading to an increase in edge parasitic excitation.

This antenna eliminates edge dissipation due to the negative helicity modes but increases that due to parasitic excitation. Another disadvantage of this arrangement is that mode number selection (a change of (n,m) mode) would demand a change of the tilt during the discharge! We therefore take the simplest choice, Fig. 6.3(a), as the starting point for the AWH antenna design for NET. The question of the modular helical antenna will be addressed again in chapter 8.

6.4 The Antenna Loading in NET

In order to compare the antenna loadings of the low field side poloidal antenna of Fig. 6.3(a) for different excited modes, we must first establish the connection between the loading due to the (n,m) mode of the travelling wave antenna used in the code and that due to the Fourier component of the poloidal antenna.

The Fourier decomposition of the current density components for a general travelling wave antenna with radial feeders is given by [6]:

$$J_r = - \text{ is } (km/r)\ \beta^{m,n}\ \Theta(r-R_A) \tag{6.2a}$$

$$J_\Theta = k\beta^{m,n}\ \delta(r-R_A) \tag{6.2b}$$

$$J_Z = -(1-s)\ (m\beta/r)^{m,n}\ \delta(r-R_A) \tag{6.2c}$$

where Θ is the Heaviside function, δ the Dirac function and $\beta^{m,n}$ is a constant. For s=0 one obtains a helical antenna and for s=1, a poloidal antenna. For N poloidal elements of the form of Fig. 6.3(a) with toroidal half angle ϕ_A, poloidal half angle θ_A and each carrying current I_0 with phases $\varepsilon_k=\pm1$ (k=1, 2,...N), it can be shown that $\beta^{m,n}$ in equations 6.2 is given by $\beta^{m,n}=\beta_0{}^{m,n}I_0$ where

$$\beta_0^{m,n} = \frac{\sin(n\phi_A)\ \sin(m\Theta_A)}{2\pi^2\phi_A\, m\, n^2} \sum_{R=1}^{N} e_k\ \exp[\frac{-i\ 2\pi\ \ n\ k}{N}] \tag{6.3}$$

If one defines the power $P_{m,n}$ delivered to the (n,m) mode as $P_{m,n}=0.5R_{m,n}I_02$ then $R_{m,n}$ is related to the load $R^{m,n}$ calculated in the kinetic code by the relation $R_{m,n}=C_{m,n}R^{m,n}$ where $C_{m,n}=4(\beta_0{}^{m,n})2$.

The antenna loading is obtained by adding the four resistances corresponding to the four combinations of $\pm m$ and $\pm n$ obtained from the code for a poloidal antenna and by multiplying by the coefficient $C_{m,n}$. We assume that $\phi\rightarrow0$, $\Theta_A=\pi/2$ and that the phases (ε_k) of the antenna elements are chosen to favourably excite the n-mode. These phasings are shown in Fig. 6.4, where N denotes the antenna phasing which favourably excites the mode n. The loading for |m|=0, 1, 3 is shown versus |n| in Fig. 6.5(a). The frequency for each |m| has been chosen to keep the ARL at the half density point. Clearly |m|=1 is the most strongly excited mode with the antenna of Fig. 6.3(a). The choice of 8 elements strongly favours the n=4 configuration at 1.08MHz and 16 elements favours n=8 at 1.98MHz (see Fig. 6.5(b)). In chapter 7 these results will be recalculated taking into account the effect of a recess.

6.5 Summary

An 8 or 16 poloidal element antenna has been chosen for AWH in NET. A large loading can be obtained by N=4 and N=8 (|m|=1) or N=16 (|m|=0) excitation.

References

[1] E. Salpietro et al., NET basic Machine, NET report (1988).
[2] K. Appert et al., Plas. Phys. and Contr. Fus. Res. Vol II (1980) IAEA-CN-38/D-1-1.
[3] Kirov et al., RF Systems for Alfven Wave Heating of Large Tokamaks, IAEA Technical Workshop on RF Heating and Current Drive, Moscow (1987).
[4] Elfimov et al., Numerical Modelling of Alfven Wave power absorption in current carrying plasma, Moscow (1987).
[5] Collins et al., Phys. Fluids 29 (1986) 2260.
[6] K. Appert et al., Introduction to the Theory of AWH, Internal report LRP 238, Lausanne (1984).
[7] G.G. Borg, PhD Thesis, University of Sydney (1987).
[8] F. Hofmann et al., Letter in Nuc. Fus. 24 No. 12 (1984) 1679.

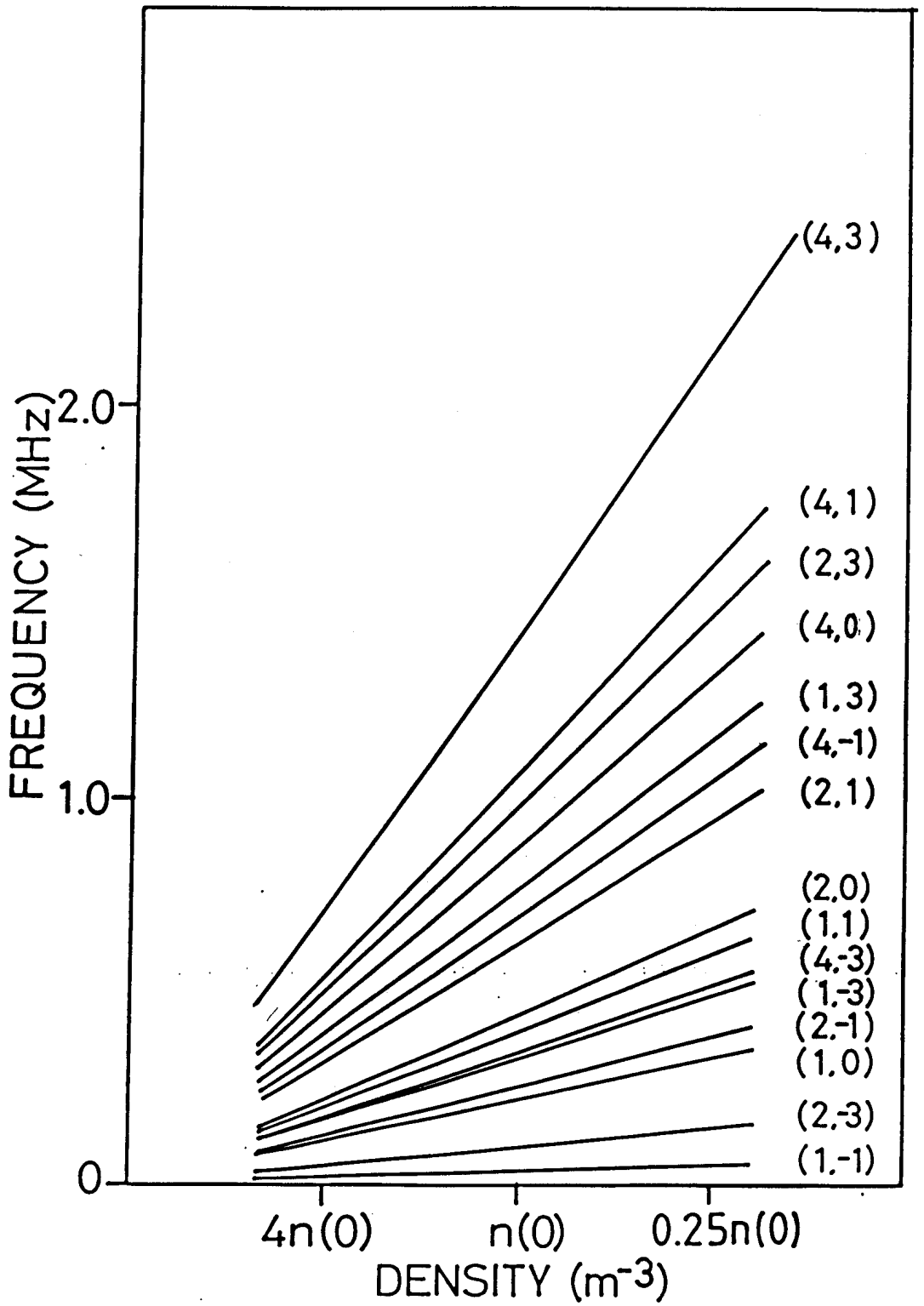

Fig. 6.1a) Frequency versus on axis density for ARLs at the half density point.

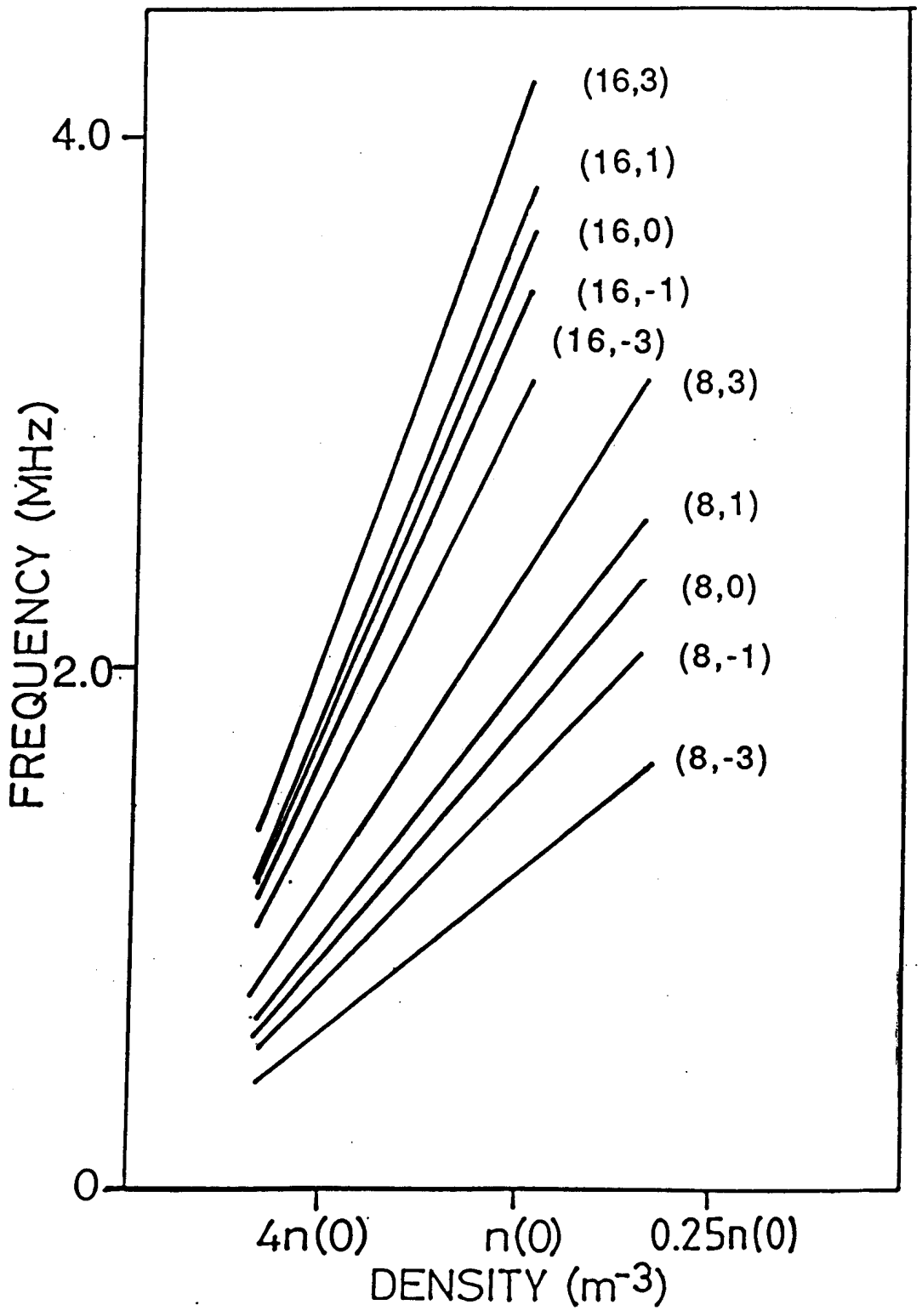

Fig. 6.1b) Frequency versus on axis density for ARLs at the half density point.

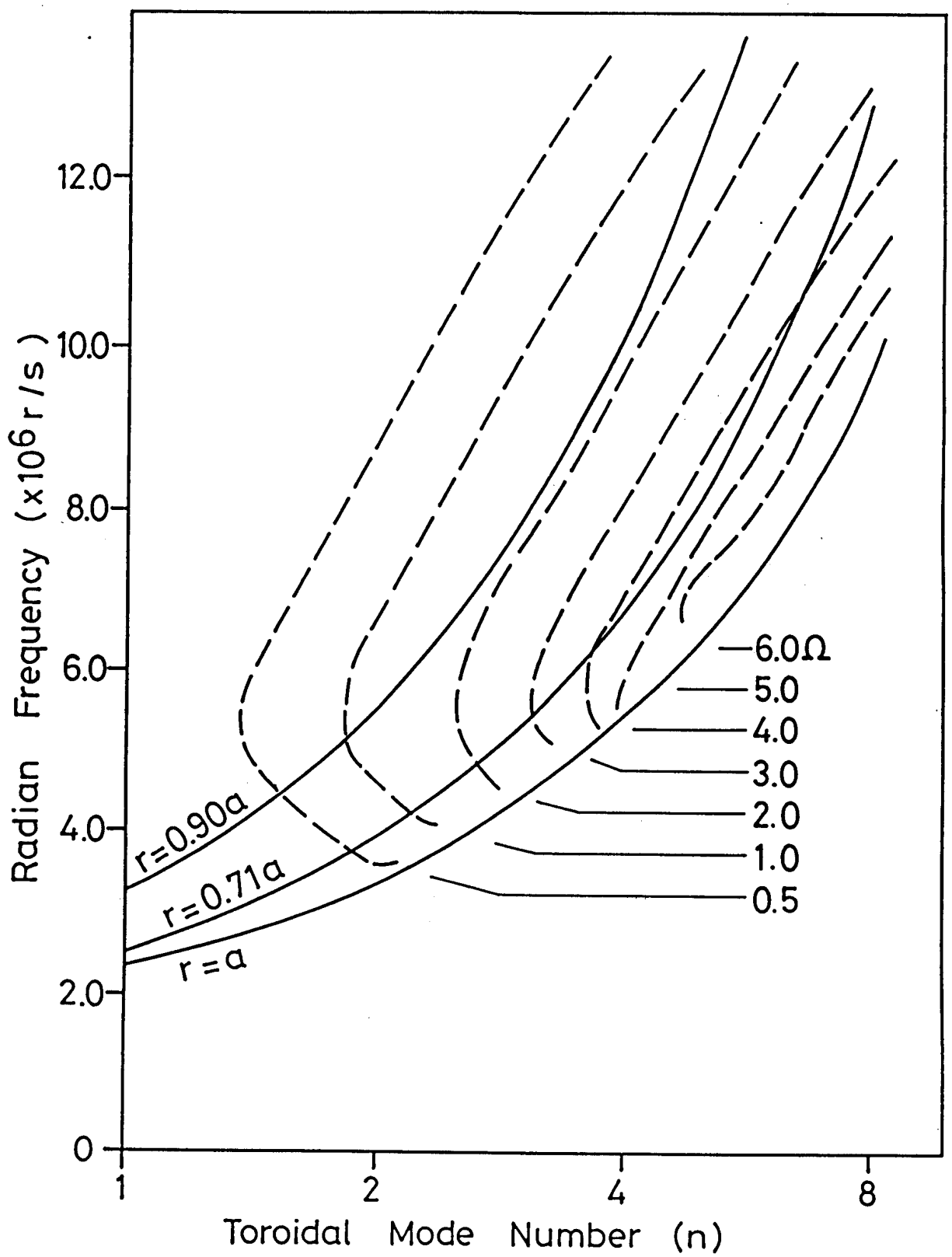

Fig 6.2 Loading contours in (ω,n) space for the m = 1, n > 0 and $n_e(0) = 17.9 \times 10^{19}$ m^{-3}.

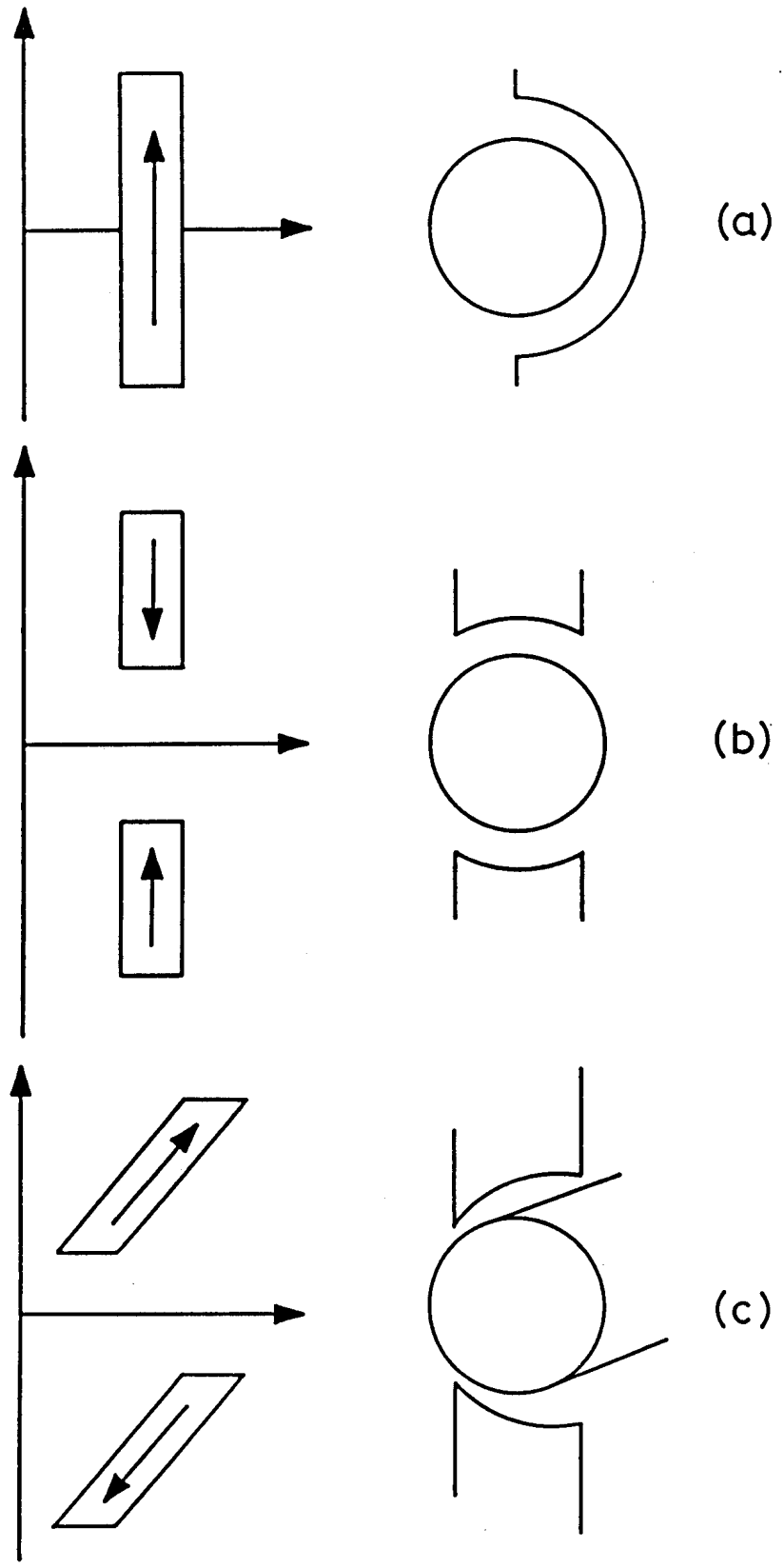

Fig 6.3 Three possible AWH antennas:

a) Low field side poloidal element.

b) Top and bottom antennas with 180^0 phasing.

c) Modular helical antenna.

+	+	+	+	−	−	−	−	N = 1
+	+	−	−	+	+	−	−	N = 2
+	−	+	−	+	−	+	−	N = 4 (a)
+	+	+	+	+	+	+	+	N = 8
+	+	+	+	+	+	+	+	N = 16

+	+	+	+	+	+	+	+	−	−	−	−	−	−	−	−	N = 1
+	+	+	+	−	−	−	−	+	+	+	+	−	−	−	−	N = 2
+	+	−	−	+	+	−	−	+	+	−	−	+	+	−	−	N = 4 (b)
+	−	+	−	+	−	+	−	+	−	+	−	+	−	+	−	N = 8
+	+	+	+	+	+	+	+	+	+	+	+	+	+	+	+	N = 16

Fig 6.4 Antenna phasings for the different excitation modes (n = 1,2,4,8,16).

a) 8 element antenna

b) 16 element antenna

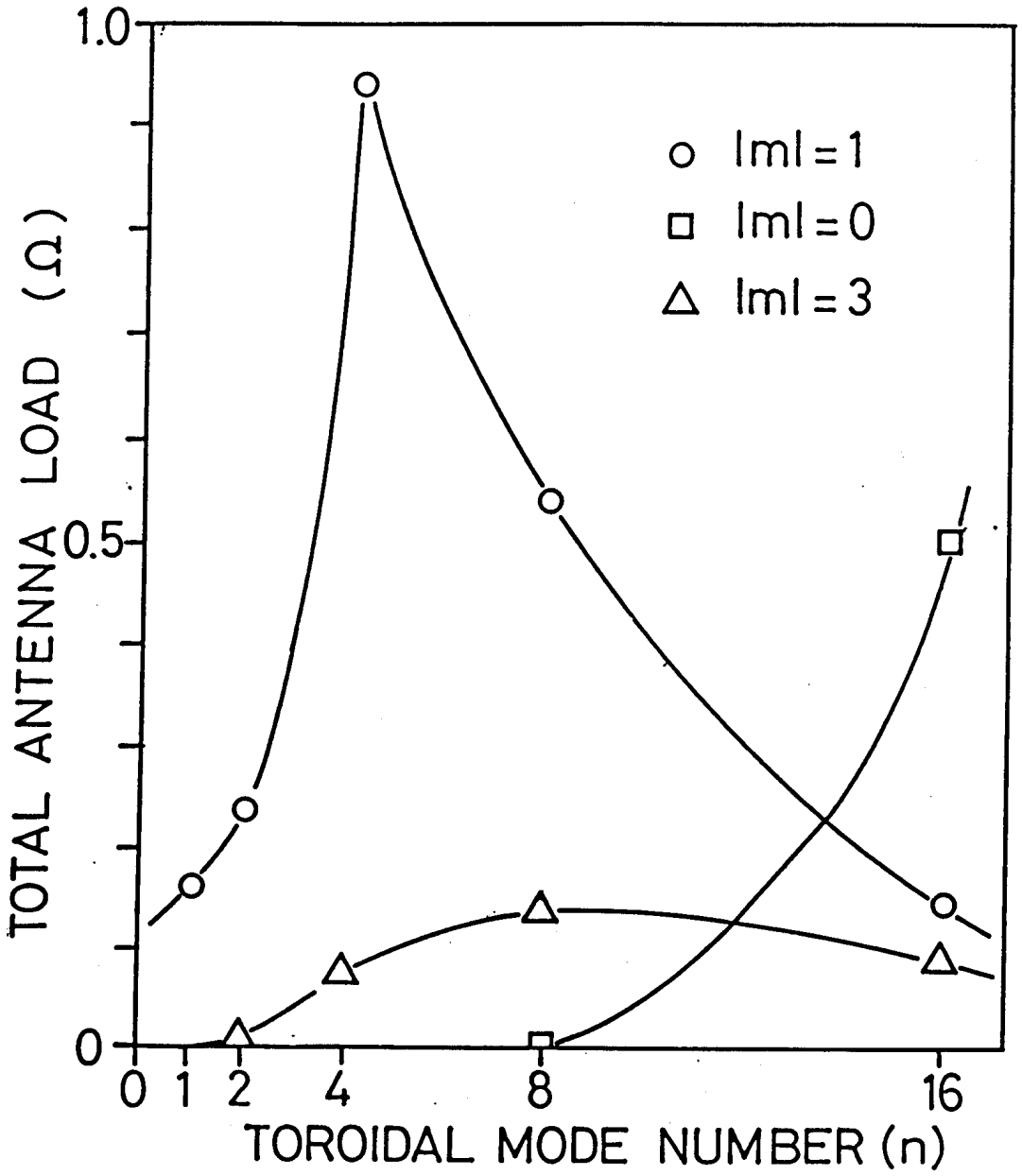

Fig 6.5a) Antenna loading versus n for m = 0,1 and 3 (8 element antenna).

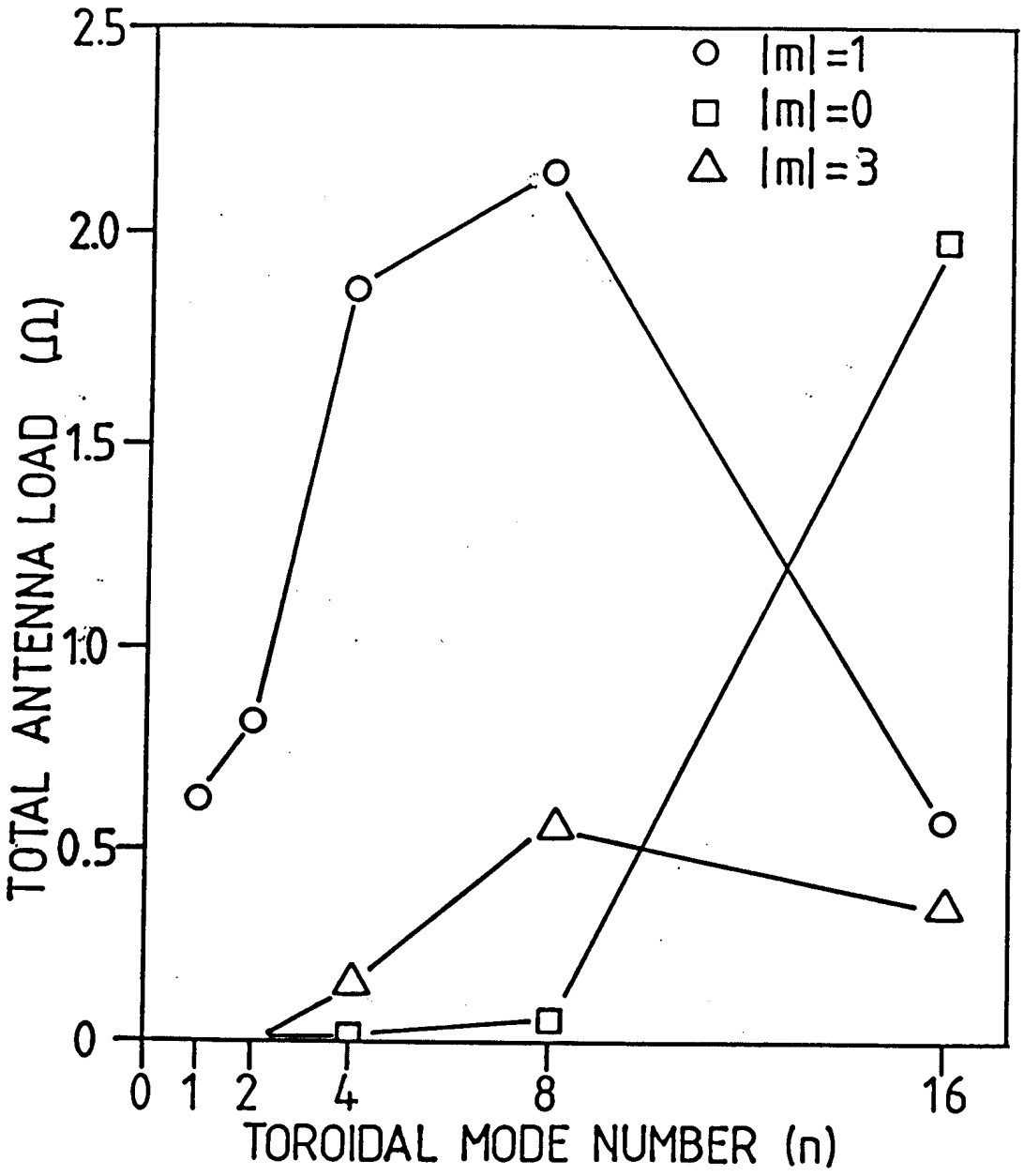

Fig 6.5b) Antenna loading versus n for m = 0,1 and 3 (16 element antenna).

7. THE ALFVEN WAVE HEATING ANTENNA IN NET

7.1 Introduction

In Chapter 6 an AWH antenna consisting of either 8 or 16 elements was proposed. The elements were assigned Θ_A=90° and ϕ_A to be optimised but in any case limited by the allowed port space. The large Θ_A (chosen to reduce high m excitation) would suggest the use of the oblique access port rather than the radial access port. The antenna is fed symmetrically and is envisaged as floating with respect to the vessel. The port space allowed (≈12°) corresponds to a total toroidal distance of 1.40m. The depth of the recess is limited to 20cm; the depth at which the blanket is located.

In Section 7.2 we consider the effect on the wave coupling and antenna electrical properties when the antenna is located in a recess to protect it from the plasma. The depth of the recess is limited to 20cm; the depth at which the blanket is located. In Section 7.3 we consider the effect of the high circulating RF currents (>10kA) on the antenna and whether the antenna can be adequately cooled. We also consider superficially the problem of high voltage breakdown and emphasize the importance of reducing the antenna self-inductance.

7.2 Calculation of the Coupling of an Antenna in a Recess

The process of launching low frequency waves necessitates placing an antenna in the region between the plasma and the vacuum chamber wall. If the plasma temperature is sufficiently high, its interaction with the antenna can release impurities into the discharge, with the combined effects of increasing the plasma loss channels and corrosion of the antenna due to sputtering of the surface material. It has therefore been proposed that such antennas be protected by placing them within a recess in the vessel wall. The advantages gained by this have been thought to outweigh the reduced antenna efficiency brought about by inducing extra currents in the vessel wall. In this section we present results of a numerical study of the change in coupling efficiency brought about by varying the antenna/wall geometry.

7.2.1 Numerical technique

We confine our attention to a region in the toroidal direction around the antenna which is much smaller that the scale length associated with toroidal curvature. In addition, we assume the antenna to be infinitely long in the poloidal direction. In the Alfvén range of frequencies the vacuum wavelength is much larger than the NET dimensions and the quasistatic approximation is therefore valid. This assumption allows us to model the antenna/wall/plasma system by electrostatics in which the conducting surfaces are replaced by a finite number of infinitely long straight conducting wires.

The numerical technique is essentially a simplified version of that used by Lehrman & Colestock [1]. As in their study, the currents are assumed to be carried by a set of elementary filaments, which each have a finite self-inductance and a mutual inductance to all the other filaments. In the present study no attempt is made to model the plasma response to the field produced by the antenna. The "plasma" is represented simply by a set of filaments. A diagram of the the arrangement of the conductors is shown in Fig. 7.1. Note that we have divided the antenna into N6 wires, the wall into a total of NW=2N3 + N4 + 2N5 wires and the "plasma" into N7 wires.

The main assumption of this chapter is that the relative scaling of the square of the Fourier coefficients of the currents in the wires which represent the plasma scale in the same way with geometry as the actual antenna loading. The quantity we desire to compute, therefore, is the current in each of the elementary filaments. We can then readily calculate the magnetic field and the antenna coupling.

Each of the conductors is divided into a set of parallel wires, each of depth δ and width w. These quantities are taken to be small enough so that the current is constant over the wire cross-section. The self-inductance of each wire is given approximately by,

$$L = 2\pi \times 10^{-7} \left[\ln\left(\frac{2l}{\delta+w}\right) + 0.5\right] \qquad (7.1)$$

where l is the length of the wire (the approximation is valid for $l \gg \delta, w$). The mutual inductance between wires i and j is given approximately by,

$$M_{ij} = 2\times10^{-7} \left[\ln\left(\frac{2l}{d_{ij}}\right) - 1 + \frac{d_{dj}}{l} - \left(\frac{d_{ij}}{l}\right)^2\right] \qquad (7.2)$$

where d_{ij} is the distance between the two wires. We assume that the resistance of the wires is equal to zero. We write the resulting matrix equation for the voltages and currents as follows:

$$\begin{bmatrix} \omega L_1 & \omega M_{12} & \cdots & \omega M_{1n} \\ \omega M_{21} & \omega L_2 & \cdots & \omega M_{2n} \\ \vdots & \vdots & \ddots & \vdots \\ \omega M_{n1} & \omega M_{n2} & \cdots & \omega L_n \end{bmatrix} \begin{bmatrix} I_1 \\ \cdot \\ I_n \end{bmatrix} = \begin{bmatrix} V_a \\ \cdot \\ V_g \\ \cdot \\ 0 \\ \cdot \\ 0 \end{bmatrix}, \qquad (7.3)$$

where I_j is the current in the i^{th} wire, V_a is the voltage across each of the antenna elements, V_g is the voltage across each of the wall elements, and n is the total number of conductors, n = N6 + NW + N7. This equation was solved using the method of [1], where the sum of the driving currents and the return currents is set equal to zero.

To compare the coupling of various geometries we calculate the Fourier transform of the x-component of the magnetic field at the surface of the plasma. To make the calculation applicable to NET, we assume that the antenna is situated on the outer radius of the NET torus. That is, we take the magnetic field to be periodic over a length $L = 2\pi R_p$, where R_p = 6.53 m (i.e. 5.18 m + 1.35 m). We write the Fourier coefficients, c_k, as follows:

$$C_k = \frac{1}{L} \int_{-\frac{L}{2}}^{\frac{L}{2}} \Lambda(x) \exp\left[-i\frac{2\pi k x}{L}\right] dx \qquad (7.4)$$

where $\Lambda(x)$ is the current per unit width at the plasma surface. Note that

we have applied Ampere's law at the plasma surface to write $B(x) \sim \Lambda(x)$. Using the N7 elements which simulate the plasma surface, we write the integral as a sum,

$$c_k = \frac{1}{L} \sum_{j=1}^{N7} I_j \exp[-i \frac{kx_j}{R_p}] \qquad (7.5)$$

where the j subscripts refer to the plasma elements.

We also wish to compute a quantity proportional to the power dissipation in the wall. For the purpose of the preceding calculation, we took the resistance of each of the current carrying elements to be zero. However, if we allow each of the wall elements to have a finite resistance, small compared with the imaginary impedance, then the dissipation will be of the following form:

$$P_{wall} = \sum_{i=1}^{NW} I_i^2/\Delta x_i \qquad (7.6)$$

where i refers to the wall elements.

7.2.2 Results

7.2.2.1 Unrecessed antenna

a) Effect of plasma/wall spacing

To provide a check of the algorithm, the following test was carried out. The recess depth was set equal to zero to provide a flat wall. The plasma/wall spacing was then increased from the antenna position outwards. It was to be expected that the Fourier coefficients would eventually saturate at the value they would have without the wall. The overall width, D7, was adjusted until the current in the elements at the ends of the "plasma" was approximately zero (i.e. at least two orders of magnitude less than the peak current). Typically this distance was less than the length, L, which appears in Eq. (7.4). Therefore, to calculate the Fourier coefficients, it was assumed that the remaining length of plasma (equal to L – D7) carried no current. In effect, this allowed the integration

limits to be changed from ±L/2 to ±D7/2.

For the moment we choose the convenient small valve for the antenna width of 0.1 m. A small value will be necessary to compare the recess calculations with the plasma code in order to calibrate the loading values. Figure 7.2 shows the result for the flat wall case. Here we have plotted the amplitude squared of the two Fourier components, c_0 and c_{32}. The boxed diagram shows the physical geometry. The following numbers of elements were used (refer to Fig. 7.1): N3 = 1, N4 = 20, N5 = 20, N6 = 30 and N7 = 100. The behaviour of the spectra is as expected, with all components saturating as the wall is moved further away. Each spectrum was monotonically decreasing from $|c_0|$ to $|c_{32}|$ and so all the intermediate components lie between the two plotted on Fig. 7.2. We can observe that the higher order components saturate at a smaller distance than the low order components. This is a result of the broadening of the current distribution in the "plasma" as the wall is moved further away; in transform space the spectrum becomes more peaked.

b) Effect of antenna/plasma spacing

We now show that the square of the Fourier coefficients scales quadratically with the distance to the vessel wall as expected. Again the recess depth was set equal to zero to provide a flat wall. The antenna/wall spacing was set at a value roughly corresponing to that of NET, in which the minor radius is R_p=1.35 m and the wall radius is R_w=1.485 m on the equatorial plane. This implies a plasma/wall spacing of D1=0.135 m. However to provide a somewhat pessimistic estimate of the coupling, we fix the plasma/wall spacing at D1 = 0.1 m. Figure 7.3 shows that as the antenna is moved closer to the wall the coupling approaches zero. This figure provides a convenient standard of comparison for the studies of the recessed configuration described below. Note the similarity of this curve to that of Fig. 5.3. We conclude that the antenna loading for all modes scales quadratically with the distance from antenna to wall in the same way as the square of the near field of the antenna.

7.2.2.2 Recessed Antenna

a) Effect of recess depth

We examined the effect of varying the depth of the recess for a fixed antenna and a plasma/wall separation equal to that of the previous section. The recess width was taken to be twice the antenna width so that D4 = 0.2 m. The antenna was flush with the wall, at a distance of D2 = 0.1 m from the plasma. The result is shown in Fig. 7.4. The distribution of elements for this run was as follows: N3 = 20, N4 = 20, N5 = 20, N6 = 10 and N7 = 70. The main conclusion here is that the coupling improves rapidly until the depth of the recess is approximately equal to the antenna/plasma separation. Any further increase of the recess depth beyond this point only improves the coupling by a relatively small amount.

b) Effect of antenna width and position

We now present results of an investigation on the effect of varying both the antenna/plasma spacing and the antenna width. The recess geometry was fixed, with the depth, D3, equal to 0.1 m and the width, D4, equal to 0.2 m. Three antenna/plasma spacings were chosen:

(i)	flush with the wall,	D2 = 0.10 m,
(ii)	outside the recess,	D2 = 0.08 m,
(iii)	inside the recess,	D2 = 0.12 m.

The antenna width was varied at each of these positions. The results are shown in Fig. 7.5. The general trend is that the coupling decreases with antenna width. For the curves labelled D2 = 0.1 and D2 = 0.12, the antenna was located inside the recess and the coupling approaches zero as the antenna width approaches the width of the recess. The curve labelled D2=0.08m was outside the recess and there is an inflexion point when the antenna width was approximately equal to the recess width.

The magnetic field lines were calculated for the three antenna spacings given above, with an antenna 10 cm in width. The results, for D2 = 0.08 m, 0.10 m and 0.12 m are shown in Fig. 7.6 (a), (b) and (c), respectively. Only the field in the immediate vicinity of the antenna has been drawn. The "squeezing" of the field as the antenna is moved further

into the recess can be clearly seen.

c) Wall dissipation

The wall dissipation (Eq. 7.6) was evaluated for each of the runs shown in Fig. 7.6. and the result is shown in Fig 7.7. Clearly, the minimum wall dissipation is achieved with thin antennas far from the wall. However, taken to its limit, this would lead to an antenna of very high inductance and, consequently, very large antenna voltages. The optimum trade-off between the antenna inductance and the antenna loading does not seem to be simply generalisable, and would be studied once the geometry was precisely known.

7.3 Antenna Voltage

In this section we consider the effect of antenna inductance, resulting in high terminal voltages and breakdown problems.

To obtain some insight into the mechanics of AWH and the relation between plasma coupling and antenna inductance we consider the case of a flat wall. For the moment, neglect the flux outside the vessel and let us consider the contribution to the inductance, L_A, due to the flux near the antenna bars within the vessel. This portion of the inductance is responsible for the coupling and we refer to it as the in-vessel inductance. Suppose we keep (n,m) and the position of the ARL constant. We also keep the geometry constant except that we move the antenna radially to alter the flux. It has already been noted in Chapters 5 and 7 that, independently of (n,m), the loading scales quadratically with the distance from the antenna to the wall for NET conditions. This effect is described by Eq. 5.2. Under these conditions $P \sim\omega(h_1-h_2)^2 I^2$, where we have retained the possibility of altering ω, should n_e or B change to alter x_0 (the position of the ARL). If A denotes the area enclosed by the antenna bars, feeds and wall then $P\sim\omega I^2A^2$, since the length of the antenna remains unaltered. We therefore obtain, to a first approximation, $P\sim\omega I^2f(L_A)$ where $A^2=f(L_A)$ is a monotonically increasing function of L_A.

The terminal voltage of the antenna is $V_A=\omega L_A I$, since $\omega L_A >> R_A=R_{ant} + R_{loss}$. Hence for a given amount of total power P delivered by each antenna

element $V_A \sim \omega L_A (P/R_{ant})^{1/2}$ and so $V_A \sim (\omega L_A^2 P/f(L_A))^{1/2}$. The relation between V_A and L_A depends on $f(L_A)$. For antennas where the length in the toroidal direction is much greater than the antenna wall distance, $f(L_A) \sim L_A^2$ and the terminal voltage is independent of L_A. For antennas whose toroidal length is less than or equal to the wall distance, $f(L_A)$ is a stronger monotonically increasing function than L_A^2, since the in-vessel inductance is relatively insensitive to the area enclosed between the antenna bar and the wall. The NET antenna, with toroidal length 10cm and antenna-wall spacing 10cm (in the cylindrical approximation), is in this latter class. Hence in NET, an increase in L_A for fixed power produces a decrease in the terminal voltage. This simple picture is valid for a flat wall, but is slightly modified with a recess as we shall see later.

Unfortunately, the feeds internal to the vessel and the external circuit are also major contributors to the inductance of the antenna and since these do not effect the coupling, we refer to this contribution as the out-of-vessel inductance. The terminal voltage can only increase as this inductance is increased for a given delivered power since the antenna current must remain constant. These two inductances do, however, lead to different breakdown voltages. The breakdown electric field within the vessel is determined only by the in-vessel inductance. This breakdown electric field therefore determines the maximum allowable power delivered to the plasma per element.

7.4 Antenna Cooling

In order to calculate the heating of the antenna we need to know the current flowing in the bars of the antenna. In Table 7.5 a summary of principal results of this chapter are provided together with the circulating currents. The simplest design along the lines of the ICRH launcher is an all-metal antenna coated with a low sputtering yield material.

We now calculate the antenna losses and heating (to an order of magnitude) when the antenna is coated in silver. A hard material with a low Z would be necessary as a final surface coating to reduce plasma impurities (for example in TCA and ASDEX a titanium nitride coating is used on the in-vacuum antenna bar surfaces).

For this simple calculation we take the antenna elements to be bars of 60cm x 1cm cross-section and 6.7 m in length (corresponding to the lowfield side perimeter). The conductivity of silver is 6.15×10^7 (mho/m) and at 1.08MHz, δ (skin depth) = 0.064mm. We assume that the current flows uniformly between the surface of the antenna and the skin depth δ. This allows us to calculate a simple resistance R_{loss}.

The power dissipated and loss resistance in each bar is given in Table 7.5 for the optimum loading results assuming 50MW delivered to the plasma. Suppose that the bars are made of solid stainless steel and neglect the power lost directly by radiation from the bars through the vacuum and by thermal conduction back through the feeds. The specific heat capacity of stainless steel is 510 J/kg/°K, and the density $8 \times 10^3 kg/m^3$, so that the temperature rise per bar is $6.1^o/s$ per MW dissipated in the bars. This amounts to a total increase of <20° for each bar after 'heating and fuelling to ignition' and 'reaching of working point phase'.

This is an extremely low temperature rise which can be totally eliminated if necessary by water cooling within the bars.

Detailed numerical calculations are now presented of the loading and the antenna voltage in the presence of a recess. Here we combine the results of Sections 6.4 and 7.1 to produce realistic values to be expected in NET.

In the following discussion we assume a recess depth of maximum 20cm from inner wall to blanket and maximum width 120cm in the toroidal direction due to port space.

Antenna loading values in the presence of a recess are obtained on the basis that the parametric dependence of the loading as a function of the distance between plasma, antenna and wall is the same as calculated by the wave code in Chapter 5, and the recess code in this chapter, for the case of no recess. These calculations have shown that for all (n,m) values the loading is independent of the plasma-antenna distance and varies as the square of the antenna wall distance (Eq. 5.2). Loading conversion factors between the two codes can therefore be calculated for one set of

values of plasma, antenna and wall radius which are automatically valid for all other sets of values. The total plasma loadings assumed are those calculated in Chapter 6 for (|n|, |m|) = (4,1), (8,1) and (16,0) for both the 8 and 16 element antennas. These data are tabulated in Table 7.1.

We assume that these conversion factors remain valid in the presence of a recess.

In order to find the optimum antenna inductance recess design, we have calculated the loading and in-vessel antenna voltages for 50 MW delivered power as a function of both recess depth and width in the toroidal direction. The antenna elements are assumed to be flush with the wall, 6.7 m in length and of toroidal width equal to half the recess width. The antenna plasma spacing is 10cm.

The results of the study are shown in Tables 7.2 to 7.5. In Table 7.2 the inductance of each element is shown as a function of recess depth and width. The inductance varies considerably, from 0.39 to 2.59μH. The trend is that the largest inductance values occur for thin elements and deep recesses and the smallest inductance values for wide elements and shallow recesses.

The (total) antenna loadings for the 8 and 16 element antennas areshown in Table 7.3. Note that the maximum antenna loading is not obtained for the same recess dimensions as the maximum antenna inductance. Maximum antenna loading occurs for large recess widths and depths and contradicts the simple picture developed in the beginning of the section. Now we see that by increasing the antenna and recess width simultaneously we can decrease the antenna inductance whilst increasing the loading. This is conducive for the production of low antenna voltages.

A second point to note is that the recess slightly favours low n in comparison to high n.

The most important conclusion from the study is that the maximum loadings here are even higher than the favourable loadings already calculated in Chapter 6. It is of interest to compare them directly. In Fig. 7.8 we have plotted the loading for (|n|, |m|) = (4.1) (element antenna) for

two cases as a function of antenna width. The first case corresponds to the top row of Table 7.3(a) with recess depth 0.2m and the second corresponds to a flat wall 0.1m from the antenna and 0.2m from the plasma. Surprisingly at 0.6 m antenna width, the loading width a recess 90% of that without a recess.

Antenna voltages for 50 MW power input are shown in Table 7.4 Generally, the voltages are dissapointingly high. The voltages for the optimum case of a recess width 1.2m and depth 0.2m and a 16 element antenna are a minimum compared with all other configurations and are quite reasonable. The main problem with the voltage calculation is that consideration has only been taken of the in-vessel inductance. Inclusion of the flux linked at the feeders will add to these voltages.

As a result, the greatest likelihood of breakdown is in the feeder tunnels of the port plugs. A study of this problem requires a more sophisticated calculation of antenna inductance including the contribution due to the feeds. In addition, engineering considerations such as the choice of insulator material supporting the feeders inside the port plug tunnels must be considered before the limiting tolerable voltages can be defined. Since the feeders do not affect plasma loadings, such a study has been considered beyond the scope of this report. Similarly we neglect to consider possible breakdown problems arising in the external circiut. One encouraging aspect of the voltages in Table 7.5 is that since the most likely point of breakdown is between the edge of the antenna and the intersection of the vessel wall and the recess, then the possibility of breakdown not only decreases due to decreasing voltage as this distance is increased but also due to the increasing distance itself.

7.5 Summary

A parametric study of the AWH antenna in a recess has been performed. Calculations summarized in Table 7.5 show that very favourable antenna loading can be obtained with a recess of depth 0.20m and width 1.20m. Antenna voltage due to in-vessel inductance for this same geometry and 50 MW input power to plasma has been calculated to be satisfactory for n=4 in particular. A more detailed engineering study of breakdown at

the feeds is necessary in order to optimise antenna design.

Antenna cooling is not a problem and may even be unnecessary.

Reference

[1] I.S. Lehrman and P.L. Colestock, Internal Report, PPL, Princeton.

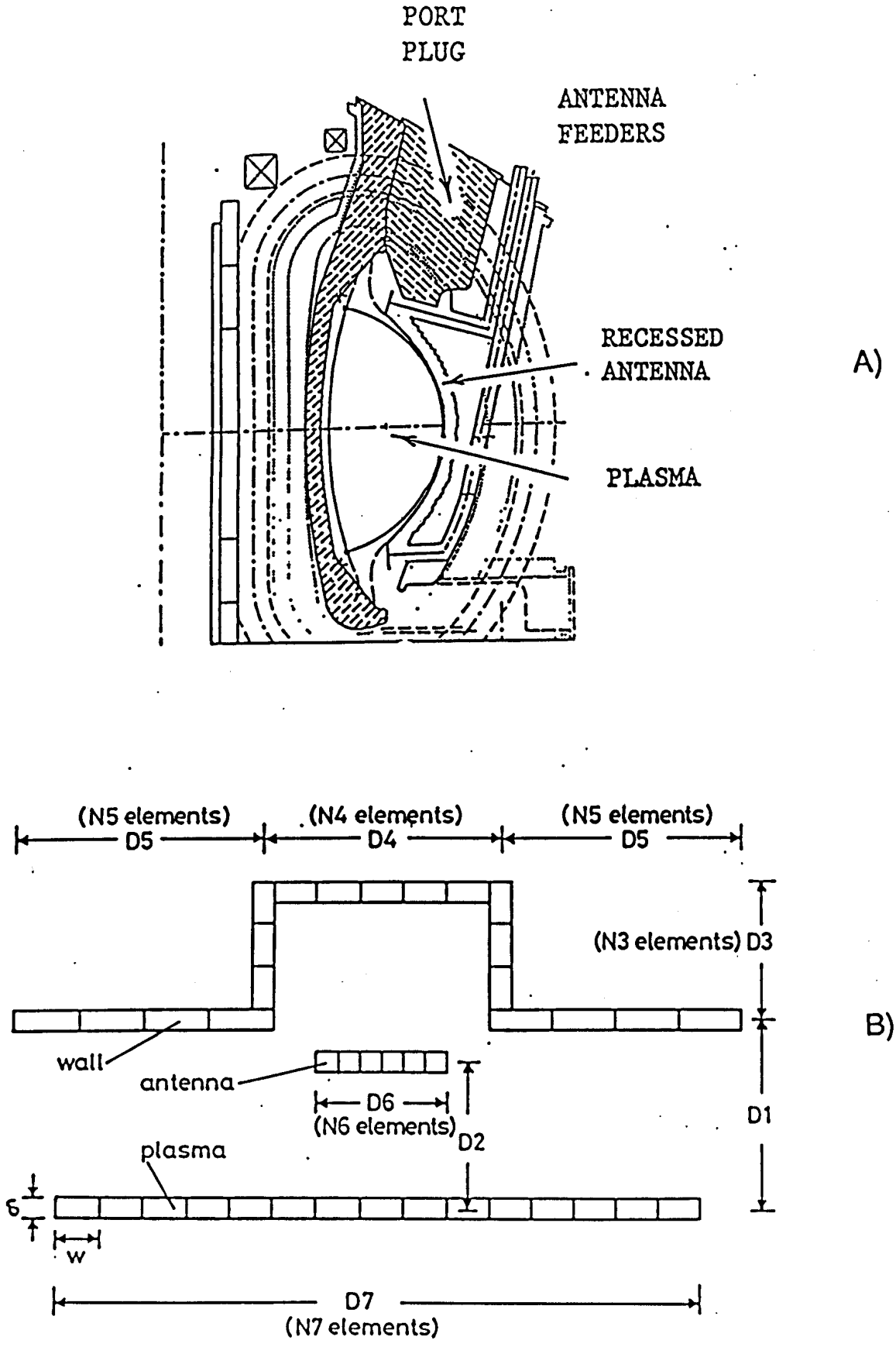

Fig 7.1a) antenna in NET oblique access port.

b) recessed antenna configuration.

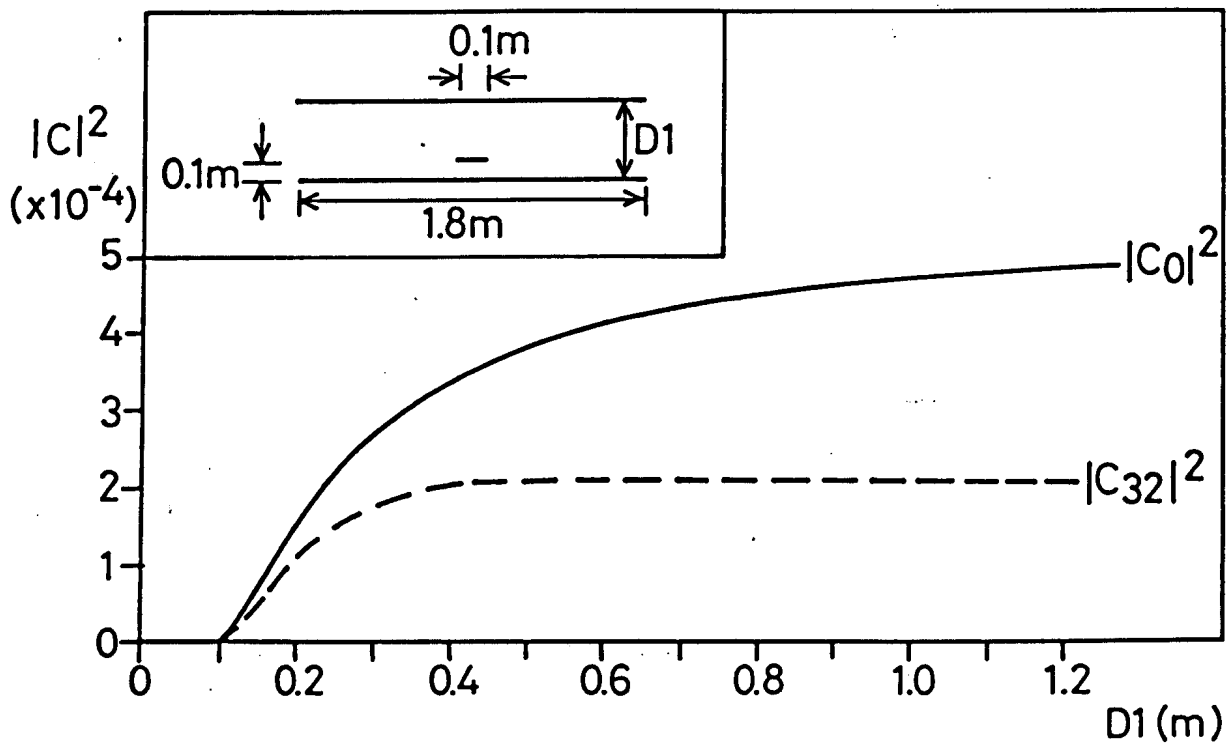

Fig 7.2 Variation of Fourier components with plasma-wall separation.

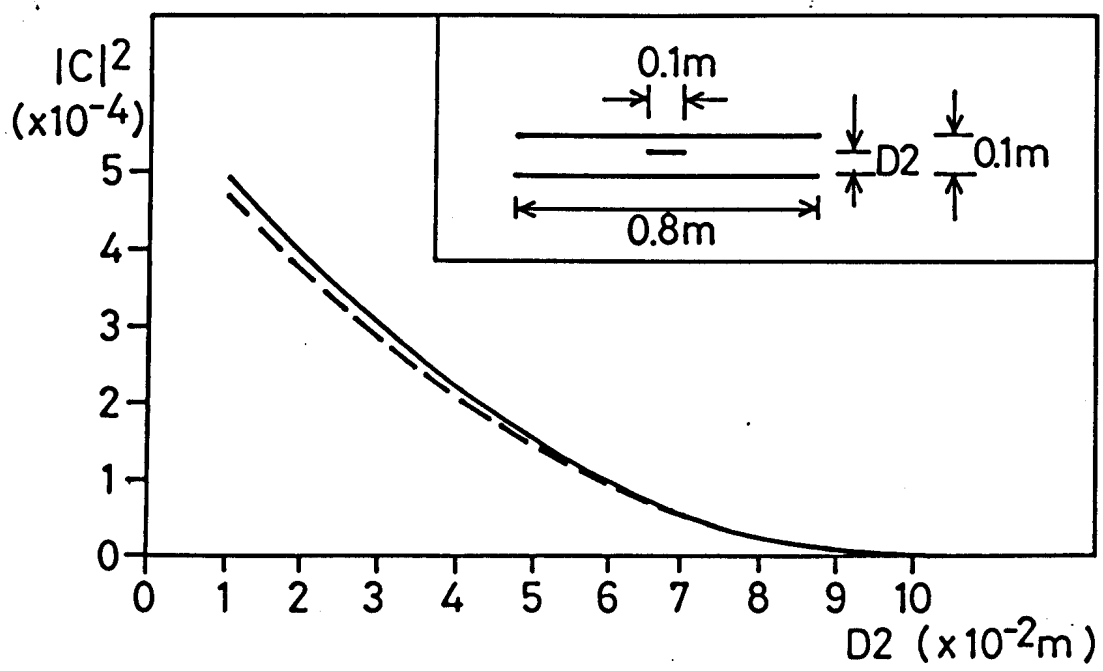

Fig 7.3 Variation of Fourier components with plasma-antenna spacing for a fixed flat wall.

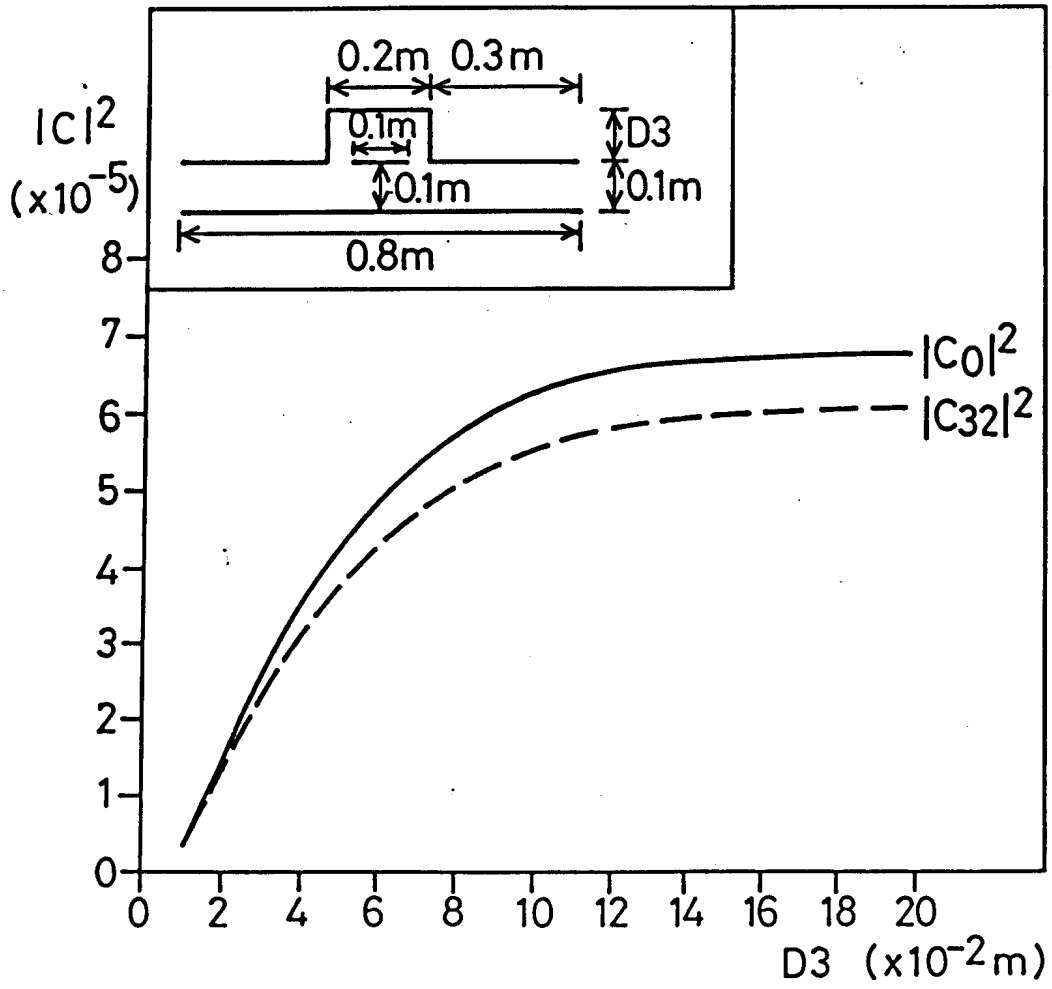

Fig 7.4 Variation of the Fourier components with recess for a fixed flush antenna.

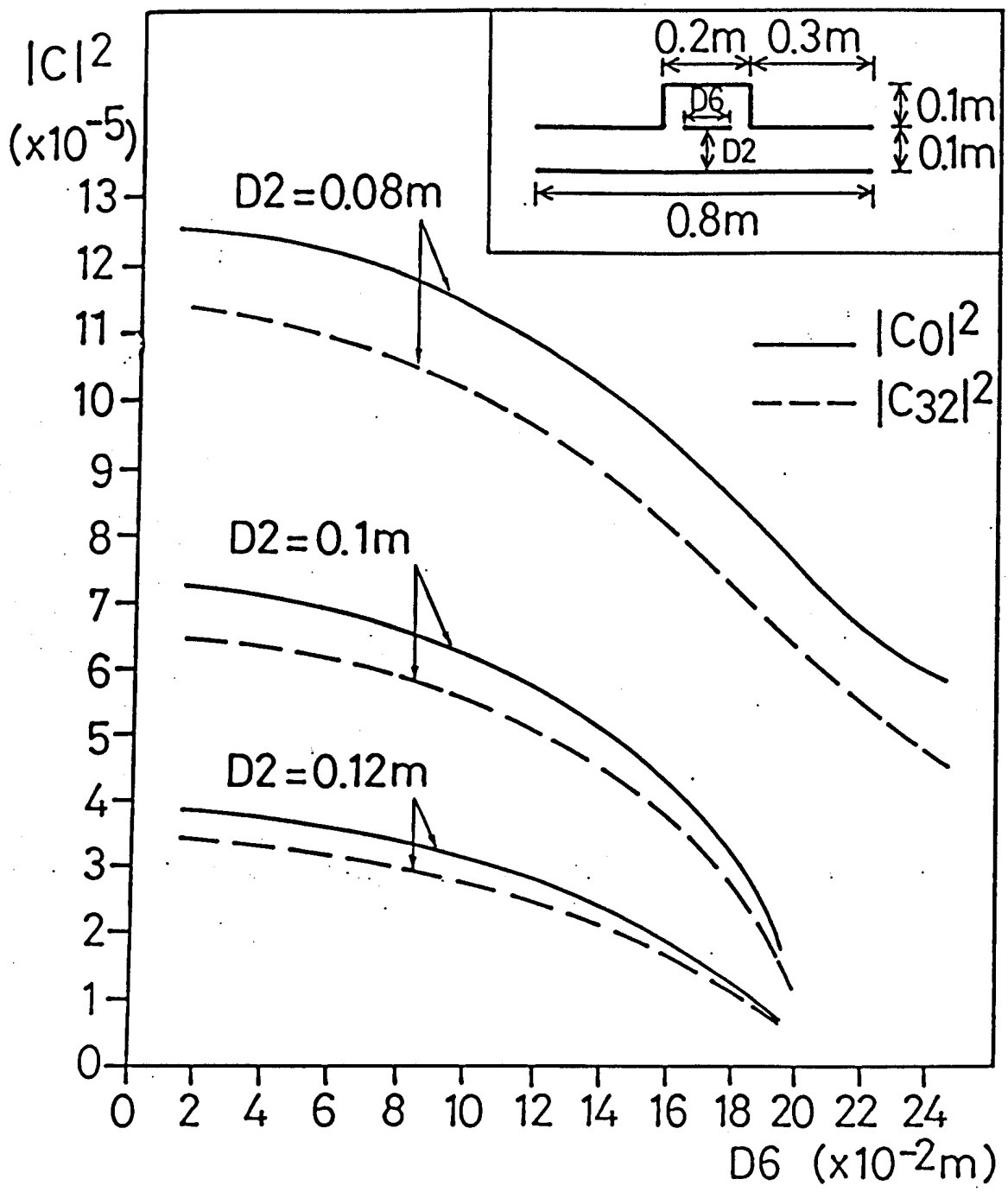

Fig 7.5 Variation of Fourier components with antenna width for three values of antenna-plasma spacing.

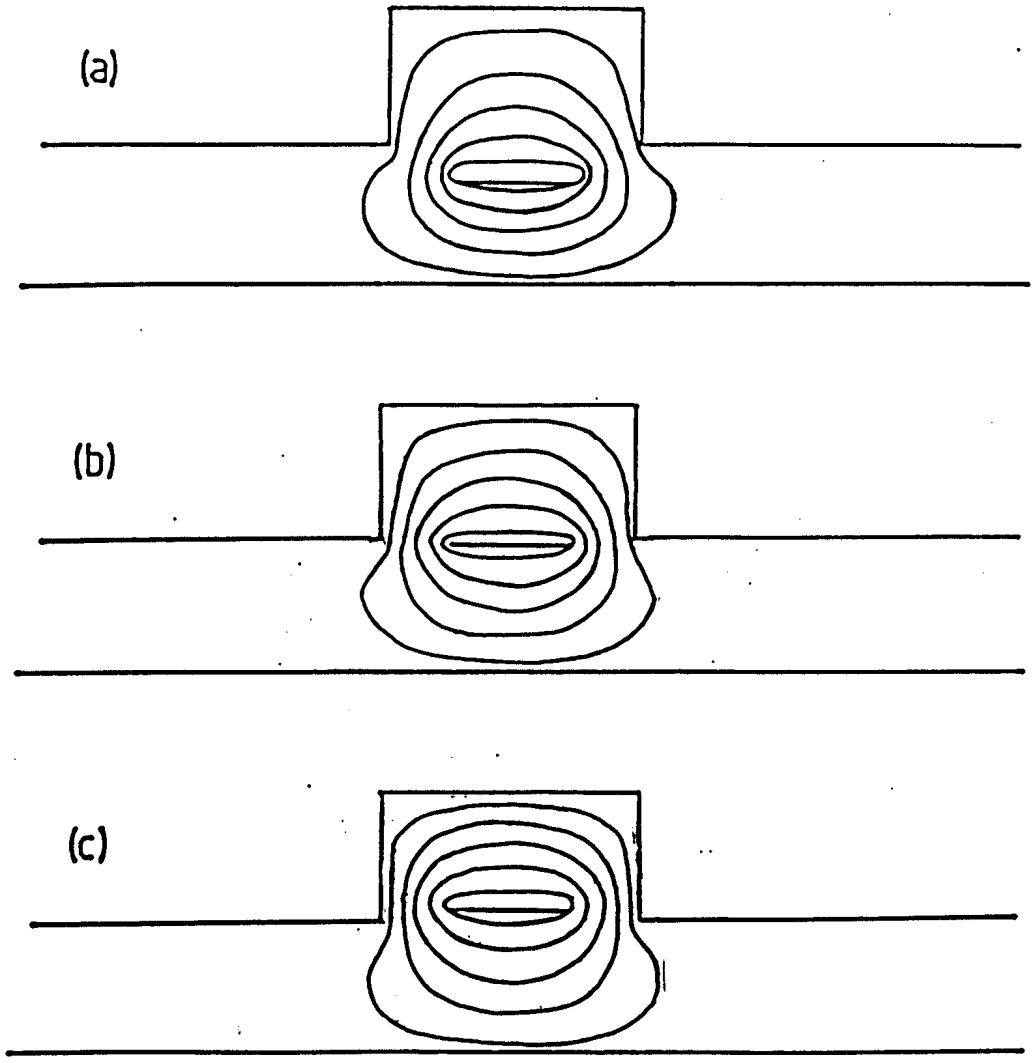

Fig 7.6 Some sample field line plots for the recessed antenna.

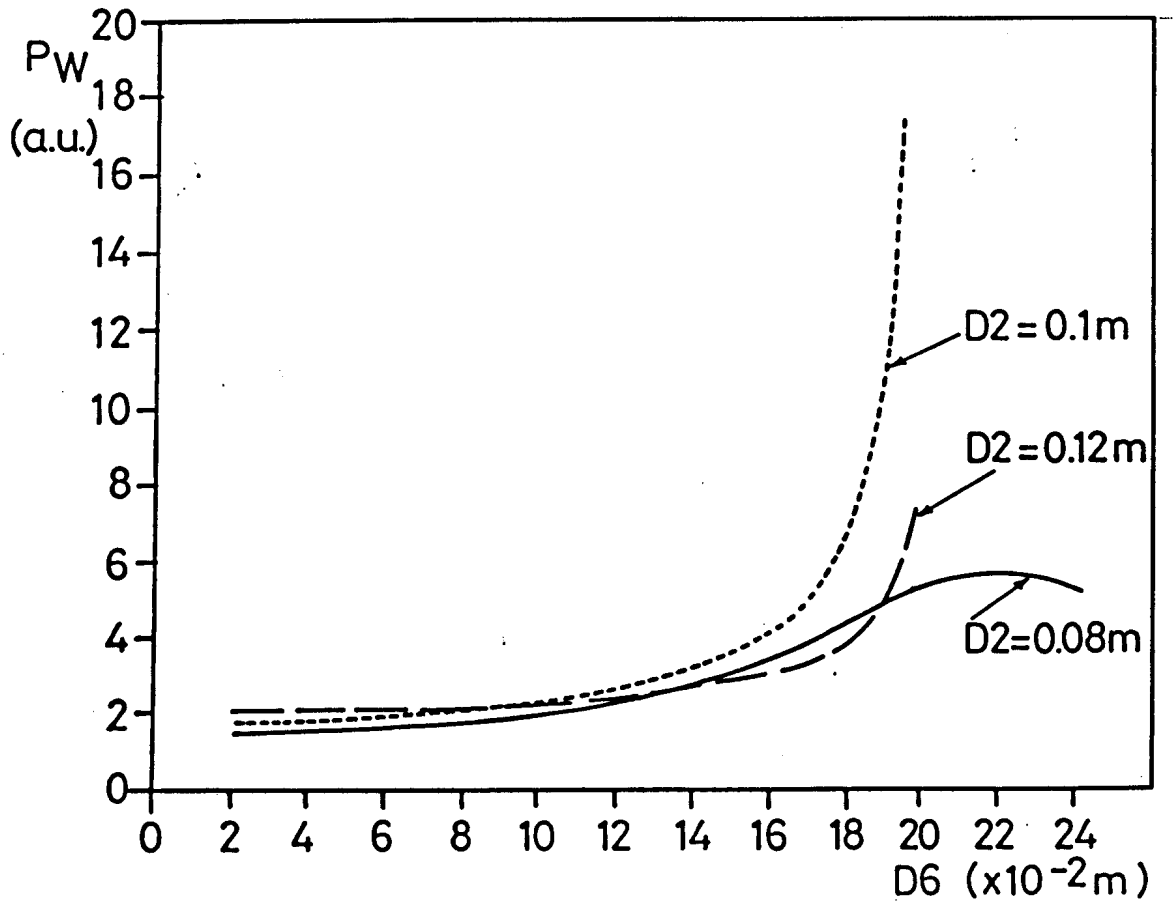

Fig 7.7 The wall dissipation as a function of antenna width for three values of antenna-wall spacing.

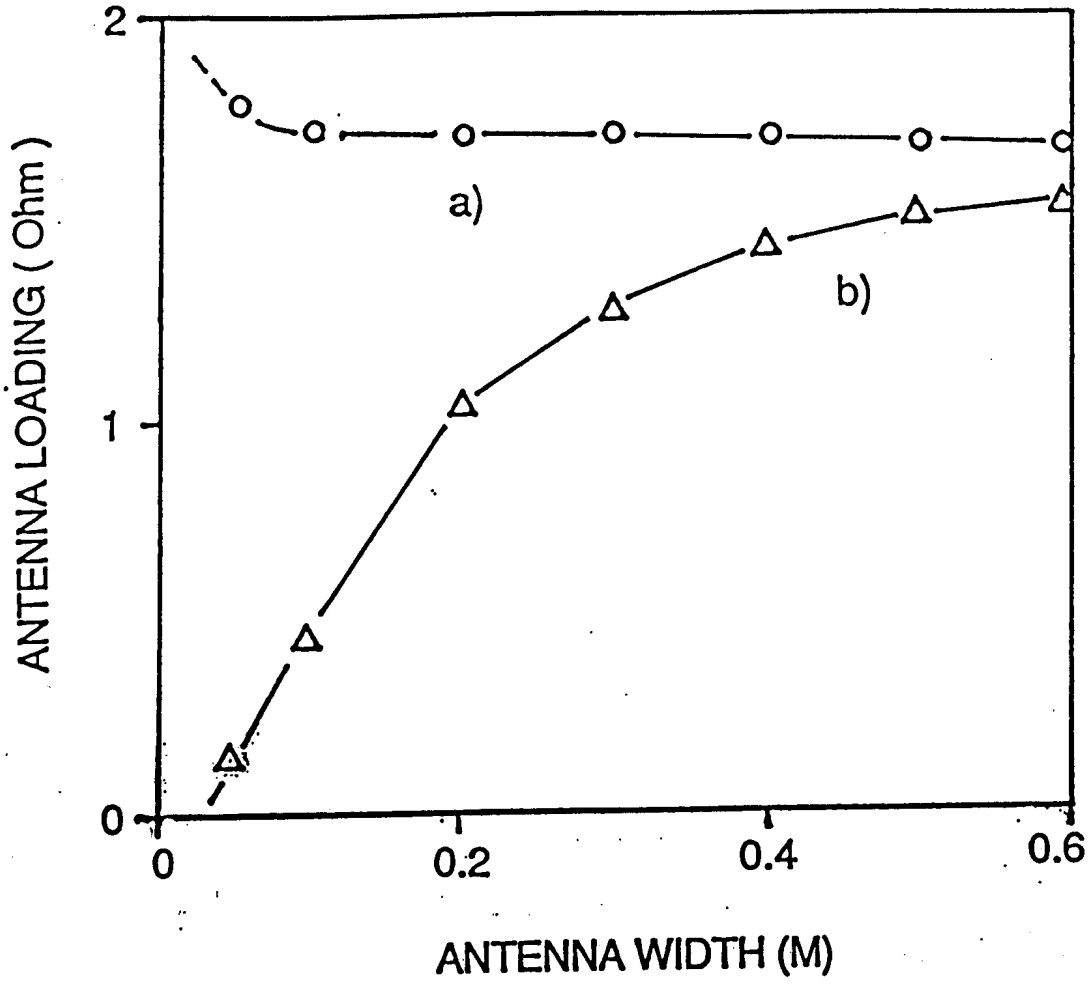

Fig 7.8 Comparison of total loading for n = 4 (8 element antenna) as a function of antenna width for the case of

a) a flat wall 10 cm from the antenna and 20 cm from the plasma and,

b) the antenna flush with the wall 10 cm from the plasma and backed by a recess of depth 0.2 m and width equal to twice the antenna width.

	(|n|, |m|)	R_{ant} (Ω)	Conv. factor
8 element	(4.1)	0.935	7.00×10^3
	(8.1)	0.537	4.09×10^3
	(16.0)	0.499	4.09×10^3
16 element	(4.1)	1.87	1.40×10^4
	(8.1)	2.14	1.63×10^4
	(16.0)	2.00	1.638×10^4

Table 7.1 Antenna loadings from Fig. 6.5 and recess code conversion factors.

		recess width (m)						
		0.1	0.2	0.4	0.6	0.8	1.0	1.2
recess depth (m)	0.2	2.59	2.60	2.04	1.76	1.41	1.18	1.03
	0.15	2.59	2.59	1.97	1.68	1.33	1.10	0.96
	0.10	2.59	2.52	1.82	1.52	1.19	0.98	0.85
	0.05	2.49	2.21	1.45	1.23	0.94	0.77	0.66
	0.01	1.46	1.06	0.77	0.75	0.54	0.44	0.39

Table 7.2 Antenna Inductances (μH)

			recess width (m)						
		(n, m)	0.1	0.2	0.4	0.6	0.8	1.0	1.2
recess depth(m)	0.2	(4, 1)	0.146	0.456	1.04	1.28	1.44	1.51	1.55
		(8, 1)	0.085	0.265	0.601	0.737	0.817	0.853	0.863
		(16, 0)	0.083	0.259	0.576	0.685	0.729	0.724	0.691
	0.15	(4, 1)	0.146	0.443	0.943	1.11	1.21	1.25	1.27
		(8, 1)	0.085	0.257	0.546	0.637	0.688	0.708	0.711
		(16, 0)	0.083	0.253	0.524	0.596	0.618	0.605	0.577
	0.10	(4, 1)	0.144	0.409	0.754	0.831	0.875	0.896	0.903
		(8, 1)	0.084	0.238	0.438	0.480	0.503	0.509	0.508
		(16, 0)	0.082	0.234	0.423	0.453	0.457	0.445	0.422
	0.05	(4, 1)	0.130	0.280	0.403	0.422	0.430	0.436	0.437
		(8, 1)	0.075	0.163	0.235	0.245	0.249	0.251	0.249
		(16, 0)	0.074	0.161	0.230	0.238	0.235	0.229	0.217
	0.01	(4, 1)	0.031	0.04	0.05	0.07	0.07	0.07	0.07
		(8, 1)	0.018	0.03	0.03	0.04	0.04	0.04	0.04
		(16, 0)	0.018	0.03	0.03	0.04	0.04	0.04	0.04

Table 7.3a Antenna Loading (Ω) 8-element antenna

recess depth (m)	(n,m)	recess width (m) 0.1	0.2	0.4	0.6	0.8	1.0	1.2
0.2	(4,1)	0.292	0.910	2.07	2.56	2.87	3.02	3.10
	(8,1)	0.339	1.06	2.39	2.94	3.26	3.40	3.44
	(16,0)	0.334	1.04	2.30	2.74	2.92	2.89	2.77
0.15	(4,1)	0.291	0.884	1.88	2.21	2.41	2.50	2.54
	(8,1)	0.337	1.03	2.17	2.54	2.74	2.82	2.84
	(16,0)	0.333	1.01	2.10	2.39	2.47	2.42	2.31
0.10	(4,1)	0.288	0.817	1.51	1.659	1.74	1.79	1.803
	(8,1)	0.335	0.951	1.75	1.91	2.00	2.03	2.026
	(16,0)	0.329	0.941	1.69	1.81	1.83	1.78	1.690
0.05	(4,1)	0.259	0.559	0.804	0.843	0.859	0.871	0.872
	(8,1)	0.301	0.651	0.935	0.978	0.993	1.00	0.994
	(16,0)	0.297	0.646	0.920	0.953	0.939	0.916	0.869
0.01	(4,1)	0.063	0.09	0.106	0.139	0.135	0.138	0.141
	(8,1)	0.073	0.10	0.126	0.166	0.162	0.167	0.169
	(16,0)	0.072	0.10	0.132	0.179	0.172	0.174	0.171

Table 7.3b Antenna loading (Ω) 16-element antenna.

recess depth (m)	(n,m)	recess width (m) 0.1	0.2	0.4	0.6	0.8	1.0	1.2
0.2	(4,1)	461	262.4	136	105	80.0	65.0	56.0
	(8.1)	1105	629	327	254	194	158	137
	(16,0)	2021	1153	605	479	372	311	279
0.15	(4,1)	461	264	138	108	82.2	66.9	57.8
	(8,1)	1106	633	331	261	199	162	141
	(16,0)	2024	1159	612	489	380	319	285
0.10	(4,1)	462	267	141	113	86.5	70.3	60.9
	(8,1)	1109	641	341	272	208	171	148
	(16,0)	2029	1171	628	508	397	331	295
0.05	(4,1)	469	284	155	128	97.4	78.8	68.3
	(8,1)	1124	680	372	307	234	189	165
	(16,0)	2057	1240	682	566	437	361	321
0.01	(4,1)	559	345	227	192	142	112	99.2
	(8,1)	1339	824	539	455	335	265	233.7
	(16,0)	2441	1483	957	798	591	471	422.1

Table 7.4a Antenna voltage (kV) 8-element antenna

		recess width (m)						
	(n,m)	0.1	0.2	0.4	0.6	0.8	1.0	1.2
0.2	(4,1)	326	185	96.3	74.7	56.6	46.0	39.7
	(8,1)	553	315	163	127.6	97.2	79.3	68.9
	(16,0)	1010	576	302	239	186	155	139
0.15	(4,1)	326	186	97.6	76.5	58.2	47.3	40.9
	(8,1)	553	317	166	130	99.7	81.5	70.8
	(16,0)	1011	579	306	244	190	159	142.3
0.10	(4,1)	327	189	101	80.2	61.2	49.7	43.1
	(8,1)	555	321	171	137	104	85.4	74.3
	(16,0)	1014	585	314	254	198	165	147.5
0.05	(4,1)	331	200	110	90.8	68.9	55.8	48.4
	(8,1)	563	340	186	154	117	95.1	82.8
	(16,1)	1027	619	341	282	218	180	160
0.01	(4,1)	395	244	160	136	100	79.6	70.2
	(8,1)	671	412	270	227	168	132	117
	(16,0)	1219	741	478	399	296	236	211

Table 7.4b Antenna voltage (kV) 16-element antenna.

	(|n|,|m|)	f(MHz)	V(kV)	ωL(Ω)	R(Ω) ant	I(kA)	R(mΩ) loss	P(kW) loss	dT/dt(^{o}K/s)
8 elements	(4,1)	1.08	56.1	7.0	1.55	8.0	1.45	46.4	0.28
	(8,1)	1.98	137.	12.8	0.863	10.7	1.96	114.	0.70
	(16,0)	3.58	279	23.2	0.691	12.0	2.63	189	1.2
16 elements	(4,1)	1.08	39.7	7.0	3.10	5.7	1.45	23.6	0.14
	(8,1)	1.98	68.9	12.8	3.44	5.4	1.96	28.6	0.17
	(16,0)	3.58	139	23.2	2.77	6.0	2.63	47.3	0.29

Table 7.5 Summary of main antenna quantities under various exciting conditions and for 50 MW into plasma. Calculations are for 6.7 x 0.60 x 0.01 m^3 antenna with a recess of depth 0.2 m and width 1.2 m. R_{ant} is the total antenna load, all other quantities are per bar.

8. OPERATION IN NET

8.1 Operation During the Current Pulse

The AWH operation in NET will be discussed on the basis of the inductive operation of NET [1], shown in Fig. 8.1. We concentrate on the plasma conditions previewed for the 'heating and fuelling phase to ignition' lasting 10sec. and 'reaching of working point' phase lasting 5sec. Since He^4 production is likely to be important, especially during the latter phase, we will discuss the evolution as a function of mass density rather than of electron density. In this way, one knows the energy deposition profile as long as one has some measure of the change in <A> with time during the heating phase. The range of mass densities in the present discussion will correspond to the 50:50 D-T mixture previously assumed and the electron density range shown in Fig. 8.1. The mass density ranges from 3 to $7 \times 10^{-7} kg/m^3$.

8.2 Alternative Operating Schemes

In Chapter 6 the antenna loading in NET was calculated for the 8 and 16 element antennas. It was shown that a significant plasma loading could be obtained (within the cylindrical approximation) for the N=4, 8 and 16 phasings.

The frequencies used place the m=0 and the n/m>0 ($m \neq 0$) ARLs at the half-density point when the NET density reaches its stationary value after the heating phase. This was necessary to compare the coupling efficiencies of the different modes under similar conditions. We now investigate the heating using these three N-phasings. The aim is to keep the ARLs somewhat central during the heating phase and to deliver the greatest possible power to the plasma. As the energy deposition normally occurs between the ARL and the plasma centre, this condition is not difficult to meet. However certain modes excited by the antenna may lie at the plasma edge and must therefore be avoided.

A scheme based on N=4,8 and 16 phasing and possible with either the 8 or the 16 element antenna is shown in Fig. 8.2(a). The N=8 phase commences the heating at 2.16 MHz with the (8,-1) and (8,1) modes entering the plasma at 1.74 and 3.58×10^{-7} kg/m^3 respectively. Because of the

choice of high N operation there is little radial separation between the positive helicity (8,1) and (-8, -1) modes and the negative helicity (-8,1) and (8,-1) modes, both of which carry most of the antenna power. Halving the frequency to 1.08 MHz at 4.74 x 10^{-7} kg/m^3 and changing the antenna phasing to N=4 allows a slightly broader but more central energy deposition profile due to the (4,1) layer. Finally, tripling the frequency to 3.24 MHz with a change to N=16 phasing at 5.43x10^{-7}kg/m^3 allows still more central heating, the (16,1) layer entering the plasma at about the "reaching of working point" phase, which should have begun at ~5.00x10^{-7}kg/m^3. We now analyse this scenario in more detail.

From Fig. 6.5 the antenna loading for m=3 is always small. This is important because the ARLs of negative helicity modes with |m|=3 are the layers most likely to be located at the plasma edge. We therefore consider modes with m=0 and |m|=1. Note that although m=0 loading is generally small in Fig. 6.5, and m=2 is not excited at all in the cylindrical approximation (m=2 is not in the spectrum of our antenna), these modes (especially m=0) are important when toroidal effects are included. The mass densities at which the |m|=0, 1, 2 modes enter the plasma for the fundamental and the first few n-harmonics and for the three phasings of the 8 and 16 element antennas are summarised in Table 8.1. The ARLs existing in the plasma for the various N-phasings are plotted in Figs 8.2(b), (c) and (d).

Consider the N=8 heating shown in Fig. 8.2 (b). In the scenario shown in Fig. 8.2 (a), N=8 heating begins at 3.00 x 10^{-7} kg/m^3 and 2.16 MHz and ends at 4.74 x 10^{-7} kg/m^3, where it is followed by N=4 heating.

TABLE 8.1

ARL Entry Densities for |m|=0,1 and 2 Modes ($x10^{-7}kg/m^3$)

8 element antenna

	N=4, f=1.08 MHz			N=8, f=2.16 MHz			N=16, f=3.24 MHz		
m	n=4	12	20	8	16	32	8	16	32
0	2.58	23.2	64.4	2.58	10.3	41.2	1.15	4.58	18.3
1	4.74	29.0	73.9	3.58	12.2	45.0	1.59	5.43	20.0
-1	1.07	18.0	55.6	1.74	8.55	37.6	0.773	3.80	16.7
2	7.56	35.5	84.1	4.74	14.3	48.9	2.11	6.36	21.7
-2	0.213	13.5	47.4	1.07	6.96	34.2	0.474	3.09	15.2

16 element antenna

	N=4, f=1.08 MHz			N=8, F=2.16 MHz		N=16, f=3.24 MHz	
m	n=4	12	20	8	24	16	32
0				2.58	23.2	4.58	18.3
1	As for			3.58	26.0	5.43	20.0
-1	8 element			1.74	20.5	3.80	16.7
2	antenna			4.74	29.0	6.36	21.7
-2				1.07	18.0	3.09	15.2

Note that the ARLs do not remain for long in the centre of the plasma and that when N=8 heating begins, the (8,-2), (8,-1) and (8,0) layers, which carry more than 50% of the antenna power, are already more than half way out. The profiles for the 8 and 16 element antenna are the same except that the 16 element antenna does not excite (16,-2).

N=4 heating commencing at $4.74x10^{-7}kg/m^3$ and 1.08MHz offers the highest antenna loading for the 8 element antenna and provides slightly more central heating. The 16 element antenna which has exactly the same profiles in Fig. 8.2(c) has a lower loading for N=4 than N=8. It is not useful to consider N=4 heating with a 16 element antenna since the amount of delivered power is reduced for little change in the location of the energy

deposition. In the case of the 16 element antenna, therefore, N=8 heating is more favourable.

For mass densities larger than about $5.00 \times 10^{-7} kg/m^3$ the heating and fuelling phase has nominally ended (see Fig. 8.1). If, however, heating at higher densities is required, a better choice than N=4 for the 8 element antenna or N=8 for the 16 element antenna would be N=16 heating at 3.24 MHz where energy deposition occurs principally by direct m=0 excitation of the fast magnetoacoustic resonance. The profiles for both the 8 and 16 element antennas are shown in Fig. 8.2(d). Note that there is significant n=8 deposition at the edge for the 8 element antenna, since the N=8 and N=16 phasings of this antenna are the same. In fact, most of the 8 element antenna power is dissipated directly at the edge. N=16 heating for the 16 element antenna, on the other hand, is more central than N=8 heating. In addition, it may be used to replace N=8 heating at a higher frequency (lower mass density) since the high principal n gives more closely spaced resonance curves for all m-modes.

In this case N=16 excitation would be at 4 MHz so the (16,0) layer enters at $3 \times 10^{-7} kg/m^3$. At this point one can reconsider the tilted helical modular antenna. If the 16 element antenna is tilted then the (8,-1) and (8,-2) modes can be eliminated. This would give efficient central $|m| = 1$ heating with an N=8 phasing. In N=16 heating there is no need to reject the negative helicity layers since the layers are close together, so that a change of phasing can occur without a change in the tilt of the antenna.

We have arrived at three possible configurations which are summarised below in sequence of increasing technological complexity.

(i) An 8 element poloidal antenna excites N=8 at 2.16 MHz commencing at $3.0 \times 10^{-7} kg/m^3$, followed by N=4 at 1.08 MHz and $4.47 \times 10^{-7} kg/m^3$. Here, there is no N=16 heating.

(ii) A 16 element poloidal antenna excites N=16 at 4.00 MHz and $3.00 \times 10^{-7} kg/m^3$ lasting the entire heating phase.

(iii) A 16 element poloidal antenna tilted to eliminate the (8,-1) mode

excites N=8 at 2.16 MHz and followed by N=16 at 3.24 MHz and $4.58 \times 10^{-7} kg/m^3$.

The antenna loading as a function of central mass density for N=4,8 and 16 excitation, with |m|=0 and 1 are shown in Fig. 8.3. For both N=4 and 8, the loading is a well-behaved function, without any sudden variation above the continuum thresholds. The loading magnitudes are approximately the same as those calculated in Chapter 6. The peaks in the loading below the continuum thresholds are evidence of discrete Alfvén waves (DAWs). The effect of these waves has not yet been experimentally determined. However, experimental measurements, as well as theoretical investigations carried out using a toroidal kinetic code (A.G. Elfimov (1988) private communication), have shown that the DAW damping rate is at least an order of magnitude larger than that predicted in the cylindrical approximation by the ISMENE code. This is due to toroidal coupling. Until a toroidal kinetic code is run with parameters appropriate for NET, it is not clear whether the DAWs will be visible on the loading traces. If the DAWs are important then experimental results seem to suggest that they, as well as the continuum thresholds, should be avoided. This would ensure that the plasma equilibrium is not disturbed by crossing the thresholds at high power. In practice this could be achieved in NET by tracking the antenna loading at low power until the DAWs have passed and the continua have entered the plasma.

Some typical energy deposition profiles are shown in Fig. 8.4 for a central mass density of $7 \times 10^{-7} kg/m^3$. At this value of mass density the energy is deposited in the outer regions of the plasma. Nevertheless the deposition is extremely localised and therefore programmable. However measurements of the plasma dynamical response indicate that the temperature profile is resilient, and is independent of the spectrum (Chapter 3). Therefore it is only important to ensure that the position of the ARL, and hence the energy deposition, is not in the scrape-off region.

We now discuss N=16 heating in more detail. As mentioned previously, one possible advantage of using Alfvén wave heating in a large tokamak may be that much higher loadings can be achieved by excitation of the magnetoacoustic resonance. In a small tokamak, this resonance is above the ion cyclotron frequency, making AWH by the magnetoacoustic resonance

impossible. Heating by direct collisional damping of the resonance can still occur, but this is in the ICRH range. In a very large tokamak, such as NET, the combination of high density and large dimensions makes magnetoacoustic resonance possible below the ion cyclotron frequency. However this is not the only consideration. The resonance must also occur at a frequency low enough to position the ARL within the plasma and not in the scrape-off. (It is simple to demonstrate that magnetoacoustic resonance cannot occur below the continuum threshold.)

The magnetoacoustic resonance densities obtained from ISMENE are shown in Table 8.2, for M=0,±1 and N=8 and 16.

TABLE 8.2

Magnetoacoustic Resonance Densities ($x10^{-7}kg/m^3$)

	M=0	M=-1	M=+1
N=8 (2.16 MHz)	8.6	14.0	14.0
N=16 (3.24 MHz)	8.3	11.0	11.0

For N=8 the magnetoacoustic resonance excites ARLs in the scrape-off. For N=16 sharp resonances occur at densities where the ARL is not too far out. These peaks can be brought down into the density range 3 - $7x10^{-7}kg/m^3$ by increasing the frequency from 3.24 to 6.1 MHz. The absolute magnitude of the peaks cannot be accurately estimated in the cylindrical approximation and, in any case, their use has yet to be experimentally investigated.

8.3 Summary

Several schemes based on heating with N = 4, 8 and 16 with the 8 and 16 element poloidal antennas have been presented. For N = 4 at 1.08 MHz a loading in the vicinity of 0.80 Ω for the 8 element antenna, and 1.60 Ω for

the 16 element antenna can be obtained. These are flat over the density range. N=8 heating at 2.16 MHz gives a flat loading of ~ 0.5 Ω for the 8 element antenna and 2.2 Ω for the 16 element antenna. N = 16 heating is possible only with a 16 element antenna. This has a more central energy deposition profile, with the possibility of exploitation of the magnetoacoustic resonance.

The frequencies chosen are, to an extent, arbitrary and the optimum choice will depend directly on the mass density evolution in the actual NET heating phase. This, in turn, will depend to some extent on the Alfvén power due to the Alfvén density rise (Section 3.2.4). A more desirable option, though much more complex, would be frequency tracking. In this case the principal resonance surface is kept close to the plasma centre as the density evolves. This may prove an advantage if the Alfvén density rise becomes a problem, since the foreseen upper limit of the density during the heating phase could be too low. Frequency tracking could be accomplished by using a feedback signal provided by the plasma density. Antenna matching would be performed in real time by a servomechanism which alters the components in the matching network.

Reference

[1] F. Engelmann et al., NET physics basis, NET Report (1988).

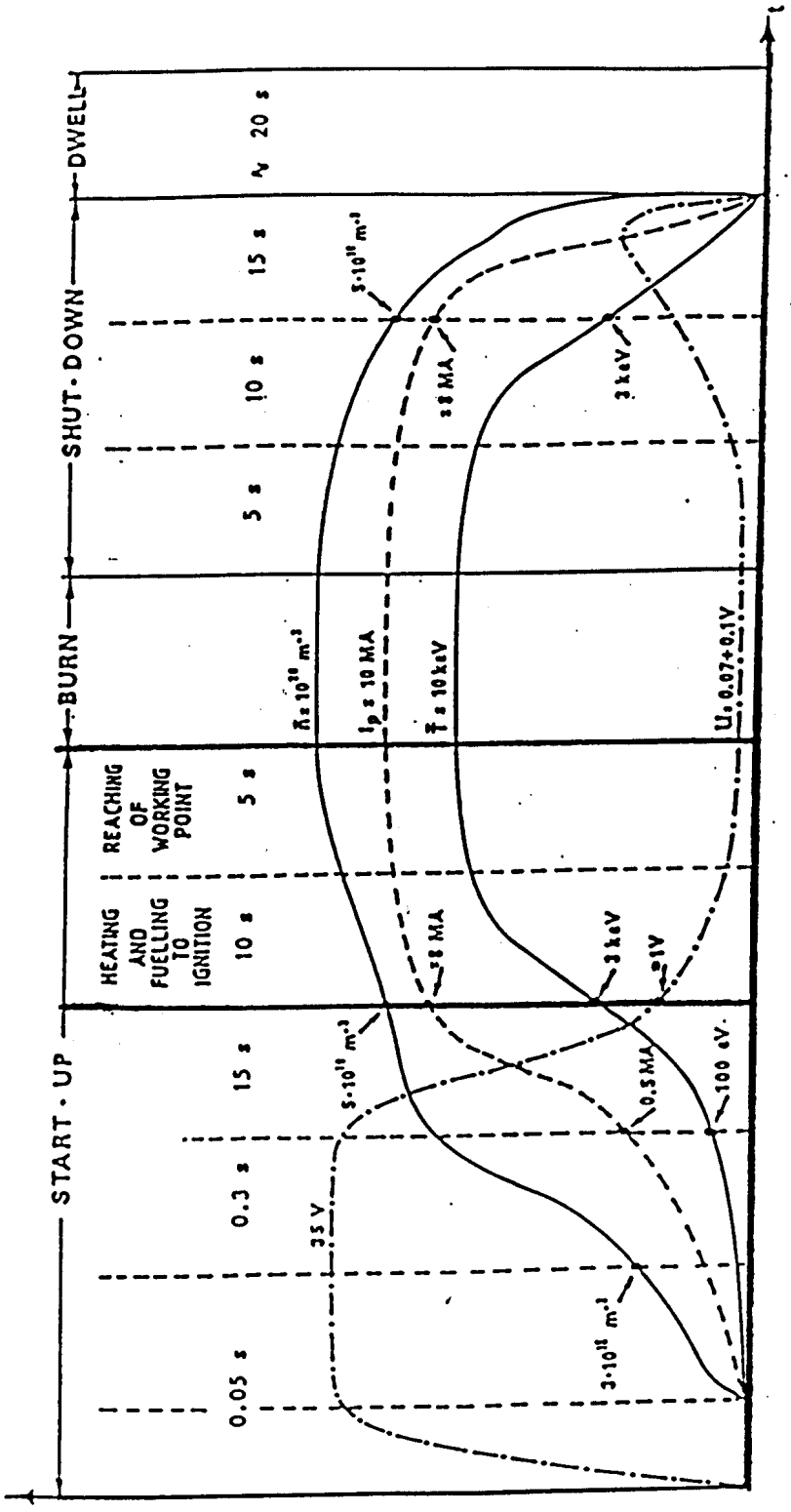

Fig 8.1 NET inductive operating scenario.

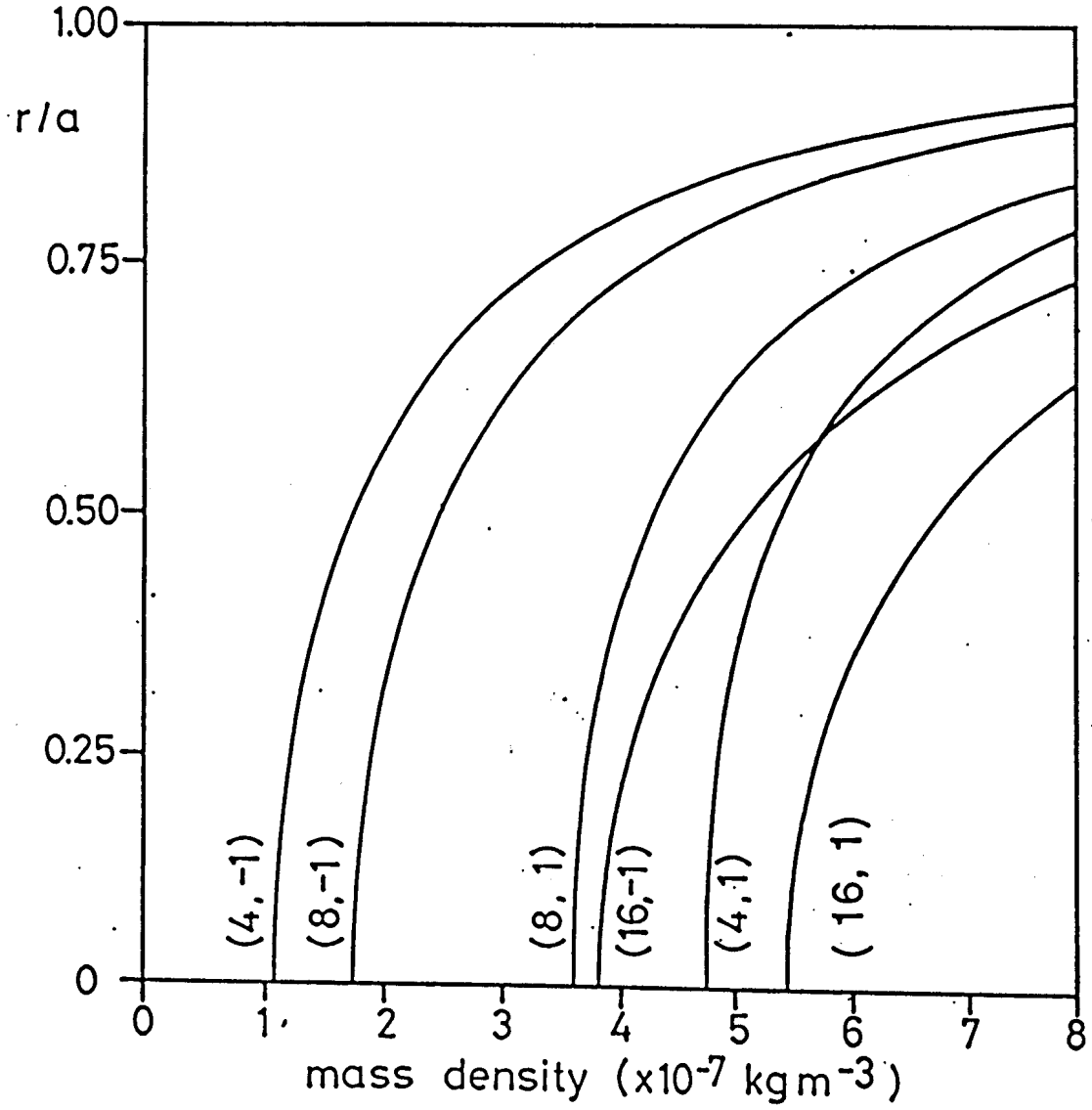

Fig 8.2a) ARL position as a function of central mass density.

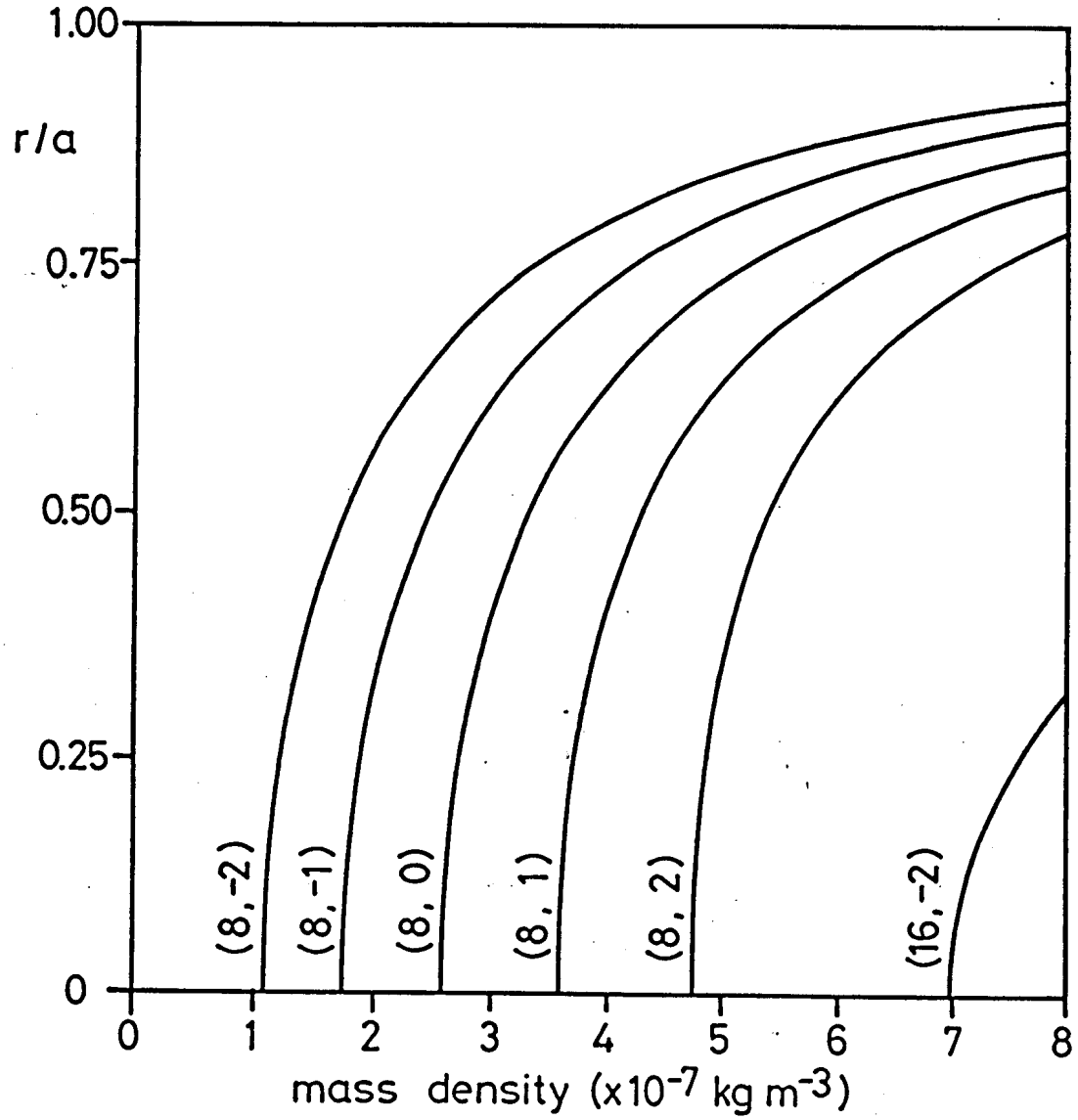

Fig 8.2b) N = 8 excitation for the 8 and 16 element antennas at f = 2.16 MHz. The (16,-2) mode is only excited by the 8 element antenna.

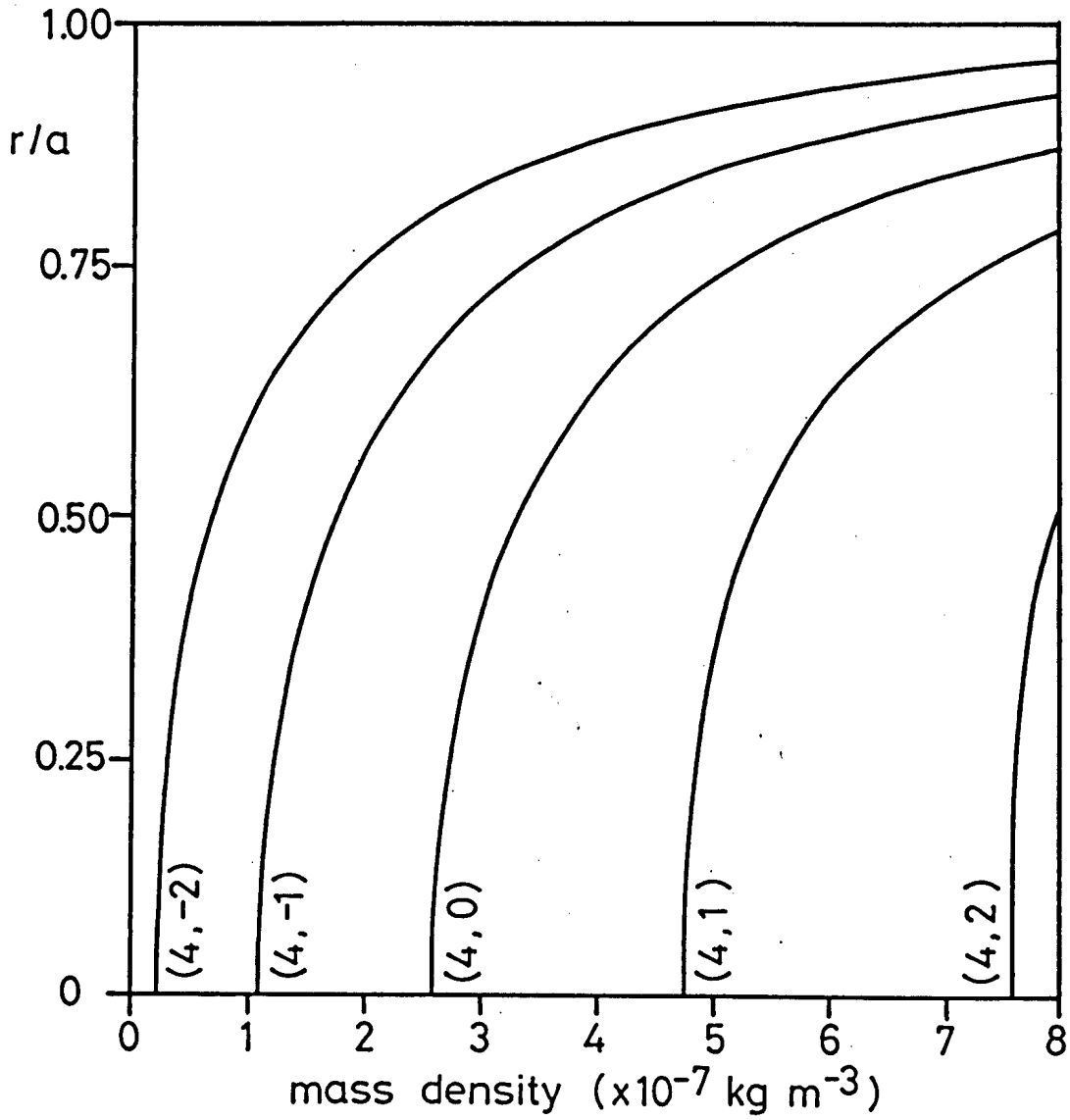

Fig 8.2c) N = 4 excitation for the 8 and 16 element antennas at f = 1.08 MHz.

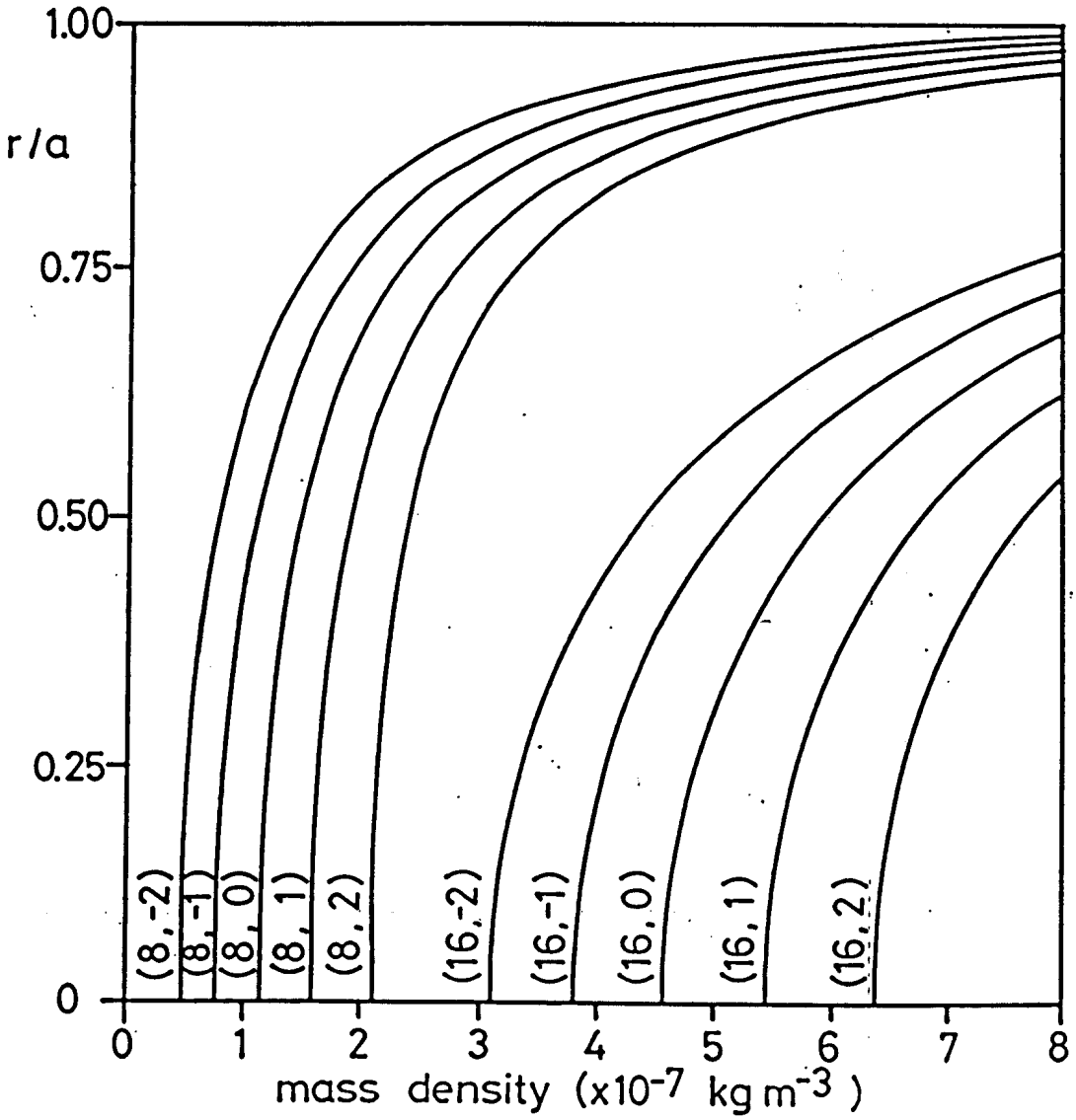

Fig 8.2d) N = 16 excitation with the 8 and 16 element antennas at f = 3.24 MHz. The n = 8 ARLs are excited only by the 8 element antenna.

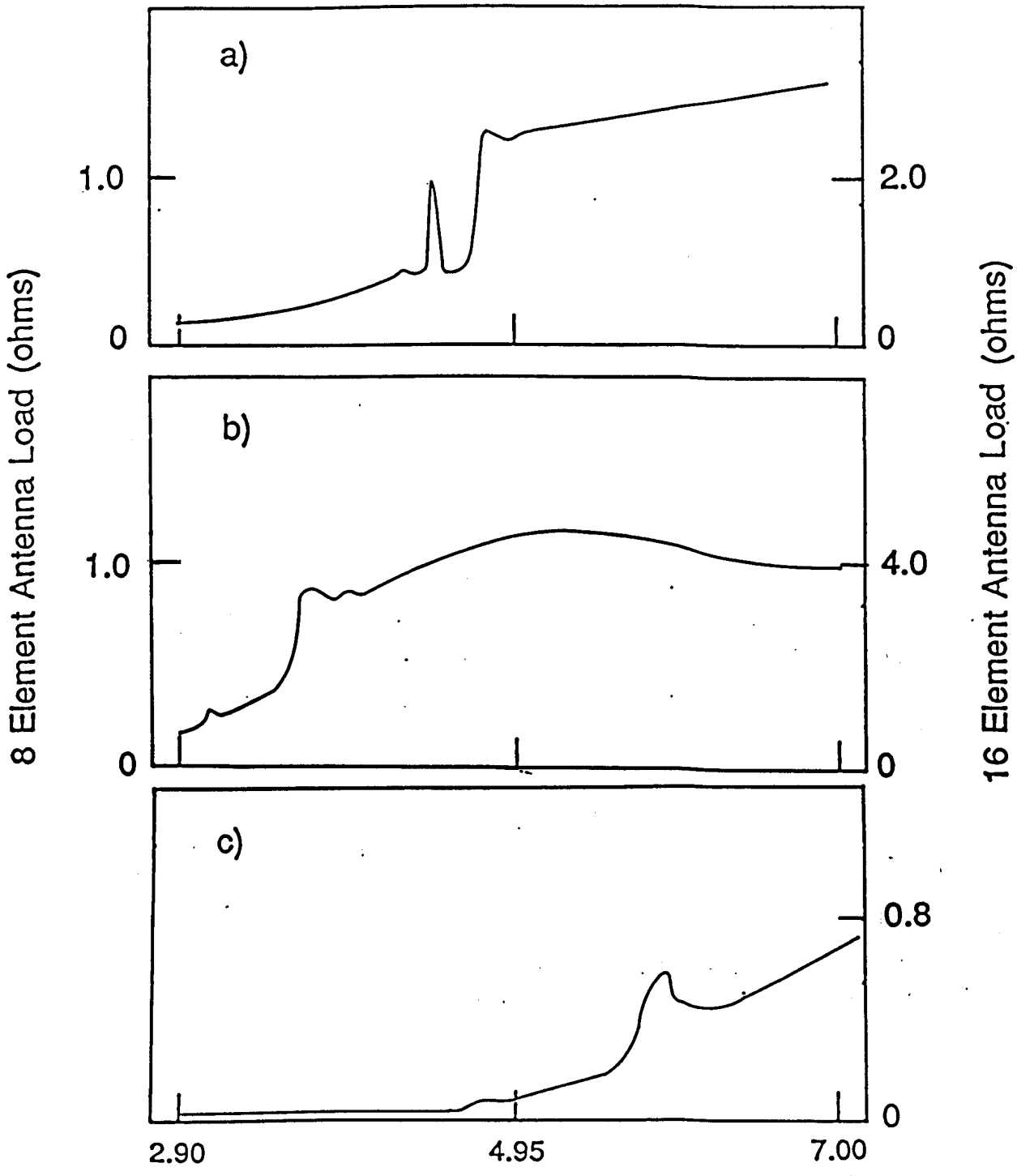

Fig 8.3 Total antenna loading for the 8 and 16 element poloidal antennas as a function of mass density during the heating phase.

a) N = 4 at 1.08 MHz.

b) N = 8 at 2.16 MHz.

c) N = 16 at 3.24 MHz.

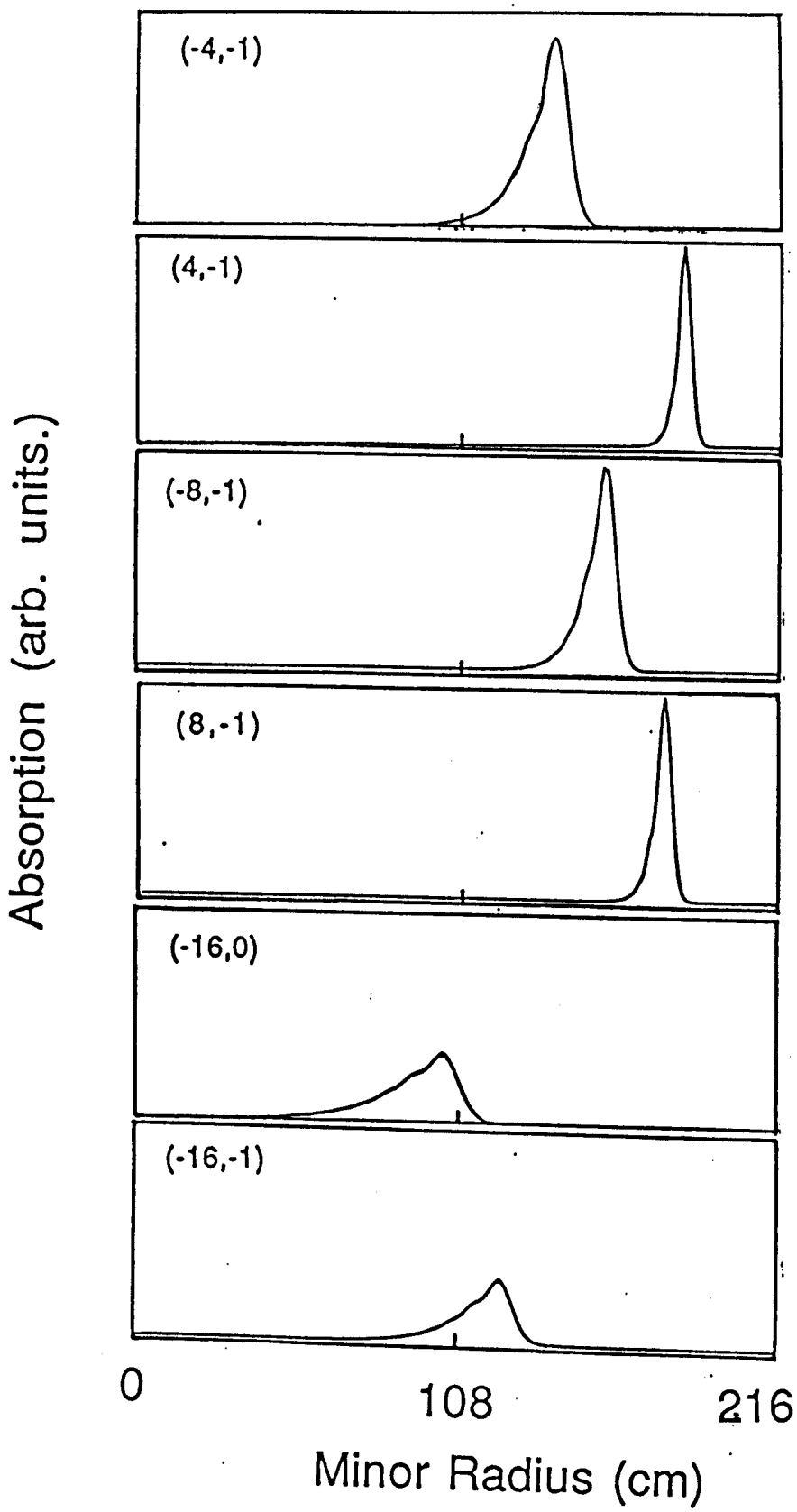

Fig 8.4 Energy deposition profiles for various (n,m) modes during the heating phase as a function of minor radius. The profiles shown are for a central density of 7.0×10^{-7} kg/m^3

9. SUMMARY

A study has been presented on the application of Alfvén waves to NET. Particular attention has been given to the use of Alfvén waves for heating. It has been shown that the antenna-plasma coupling scales from small to large tokamaks according to the simple scaling of ideal MHD and that the loading obtained is adequate for a practical heating system (Chapter 5). The operating frequency range and optimum toroidal mode numbers N=4, 8 and 16 were found, with loading estimates of 1 and 2 Ω for 8 and 16 element poloidal antennas, respectively (Chapter 6).

In Chapter 7 it was shown that only a modest degradation in loading would result if the antenna were placed in a recess. It was also shown, using the loading estimates of Chapter 6, that with a delivered power of 50 MW into the plasma, the antenna voltages and antenna heating were within tolerable limits. Finally, several possible heating schemes were discussed in Chapter 8, for N = 4, 8 and 16 and the 8 and 16 element poloidal antennas.